

The Pretornadic Phase of the Goshen County, Wyoming, Supercell of 5 June 2009 Intercepted by VORTEX2. Part I: Evolution of Kinematic and Surface Thermodynamic Fields

PAUL MARKOWSKI, YVETTE RICHARDSON, AND JAMES MARQUIS

Department of Meteorology, The Pennsylvania State University, University Park, Pennsylvania

JOSHUA WURMAN, KAREN KOSIBA, AND PAUL ROBINSON

Center for Severe Weather Research, Boulder, Colorado

DAVID DOWELL

NOAA/Earth System Research Laboratory, Boulder, Colorado

ERIK RASMUSSEN

Rasmussen Systems, Mesa, Colorado

ROBERT DAVIES-JONES*

NOAA/National Severe Storms Laboratory, Norman, Oklahoma

(Manuscript received 23 November 2011, in final form 5 March 2012)

ABSTRACT

The authors analyze the pretornadic phase (2100–2148 UTC; tornadogenesis began at 2152 UTC) of the Goshen County, Wyoming, supercell of 5 June 2009 intercepted by the second Verification of the Origins of Rotation in Tornadoes Experiment (VORTEX2). The analysis relies on radar data from the Weather Surveillance Radar-1988 Doppler (WSR-88D) in Cheyenne, Wyoming (KCYS), and a pair of Doppler-on-Wheels (DOW) radars, mobile mesonet observations, and mobile sounding observations.

The storm resembles supercells that have been observed in the past. For example, it develops a couplet of counter-rotating vortices that straddle the hook echo within the rear-flank outflow and are joined by arching vortex lines, with the cyclonic vortex becoming increasingly dominant in the time leading up to tornadogenesis. The outflow in the hook echo region, where sampled, has relatively small virtual potential temperature θ_v deficits during this stage of evolution. A few kilometers upstream (north) of the location of maximum vertical vorticity, θ_v is no more than 3 K colder than the warmest θ_v readings in the inflow of the storm. Forward trajectories originating in the outflow within and around the low-level mesocyclone rise rapidly, implying that the upward-directed perturbation pressure gradient force exceeds the negative buoyancy.

Low-level rotation intensifies in the 2142–2148 UTC period. The intensification is preceded by the formation of a descending reflectivity core (DRC), similar to others that have been documented in some supercells recently. The DRC is associated with a rapid increase in the vertical vorticity and circulation of the low-level mesocyclone.

* Emeritus.

Corresponding author address: Dr. Paul Markowski, Department of Meteorology, The Pennsylvania State University, 503 Walker Building, University Park, PA 16802.
E-mail: pmarkowski@psu.edu

1. Introduction

The 5 June 2009 tornadic supercell in Goshen County, Wyoming, is among the best-sampled storms intercepted by the second Verification of the Origins of Rotation in Tornadoes Experiment (VORTEX2; Wurman et al. 2012). The storm developed from a cluster of cells that

2100 UTC 5 June 2009
MSLP, θ_v

2131 UTC 5 June 2009
GOES-12

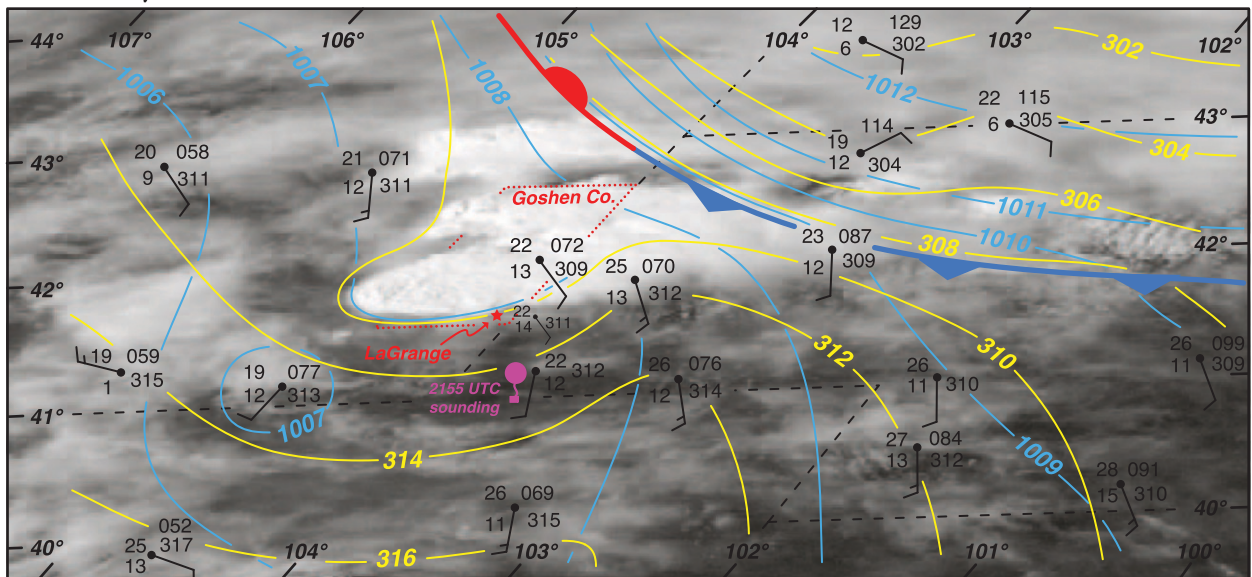


FIG. 1. Subjective analyses of mean sea level pressure (MSLP; blue contours every 1 hPa) and virtual potential temperature (θ_v ; yellow contours every 1 K) at 2100 UTC 5 Jun 2009. Station models also are valid at 2100 UTC and indicate surface temperature ($^{\circ}\text{C}$), dewpoint ($^{\circ}\text{C}$), virtual potential temperature (K), and mean sea level pressure (in tenths of hPa; the decimal and leading “10” are omitted), going counterclockwise from the top left of the station model. Winds are in kt (half barb = 2.5 m s^{-1} ; full barb = 5 m s^{-1} ; where $1 \text{ kt} = 0.5144 \text{ m s}^{-1}$). A surface front also has been analyzed using conventional symbology. The visible satellite image is from *Geostationary Operational Environmental Satellite 12 (GOES-12)* and was obtained at 2131 UTC. State boundaries are dashed black lines. Goshen County is outlined with a red dotted line. The locations of LaGrange, Wyoming, and the 2155 UTC NSSL1 sounding (see Fig. 2) also are indicated. (The 1007-mb and 310-K contours have been “diverted” around the south side of the Goshen County storm based on the assumption that outflow exists at low levels in the wake of the convection. It is presumed that the outflow is characterized by relatively low temperatures and high pressure.)

was initiated over the southern Laramie Mountains north-northwest of Cheyenne, Wyoming, shortly after 2000 UTC, in a region of south-southeasterly upslope flow at the surface (Fig. 1). The convection formed within seasonably strong west-southwesterly winds in the mid- to upper troposphere (Figs. 2a,b) associated with an approaching upper-level trough. The vertical wind profile was characterized by significant shear (e.g., the 0–3-km storm-relative helicity and magnitude of the 0–6-km vector wind difference were $\sim 170 \text{ m}^2 \text{ s}^{-2}$ and $\sim 30 \text{ m s}^{-1}$, respectively; Fig. 2b), and the convective available potential energy (CAPE) inferred from nearby soundings was roughly $2000\text{--}3000 \text{ J kg}^{-1}$, depending on which parcel’s ascent was analyzed on a thermodynamic diagram (Fig. 2a).

The storm began exhibiting supercellular characteristics (e.g., a reflectivity appendage on the right rear flank at low levels, and cyclonic azimuthal wind shear in the radial velocity data at midlevels) shortly after 2100 UTC (Figs. 3a–c), which was approximately the time that the VORTEX2 scientists made the decision to target the storm. Coarse-resolution (fine-resolution) dual-Doppler lobes were established by VORTEX2 mobile radars at

2130 UTC (2142 UTC) (Fig. 4), and mobile mesonet probes reached the precipitation region of the storm by 2140 UTC. A prominent hook echo was evident in Doppler-on-Wheels (DOW; Wurman et al. 1997) reflectivity observations by 2130 UTC (Fig. 3d). Rotation rapidly increased after 2142 UTC (a “coiled” hook echo was apparent by 2148 UTC; Fig. 3f) and reached tornado strength by 2152 UTC. The tornado, which tracked through the center of the region of dual-Doppler radar coverage (Fig. 4), intensified in the 2152–2202 UTC period, reached a maximum intensity of EF2 per mobile radar observations (Wakimoto et al. 2011; Kosiba et al. 2012, manuscript submitted to *Mon. Wea. Rev.*) and eventually dissipated at 2230 UTC near LaGrange, Wyoming.¹

This article is part of a series of articles on the Goshen County storm. The pretornadic phase of the storm (2100–2148 UTC) is treated in the present paper, as well as in a companion paper (Markowski et al. 2012,

¹ The Goshen County storm also has been referred to as the “LaGrange storm” (e.g., Wakimoto et al. 2011).

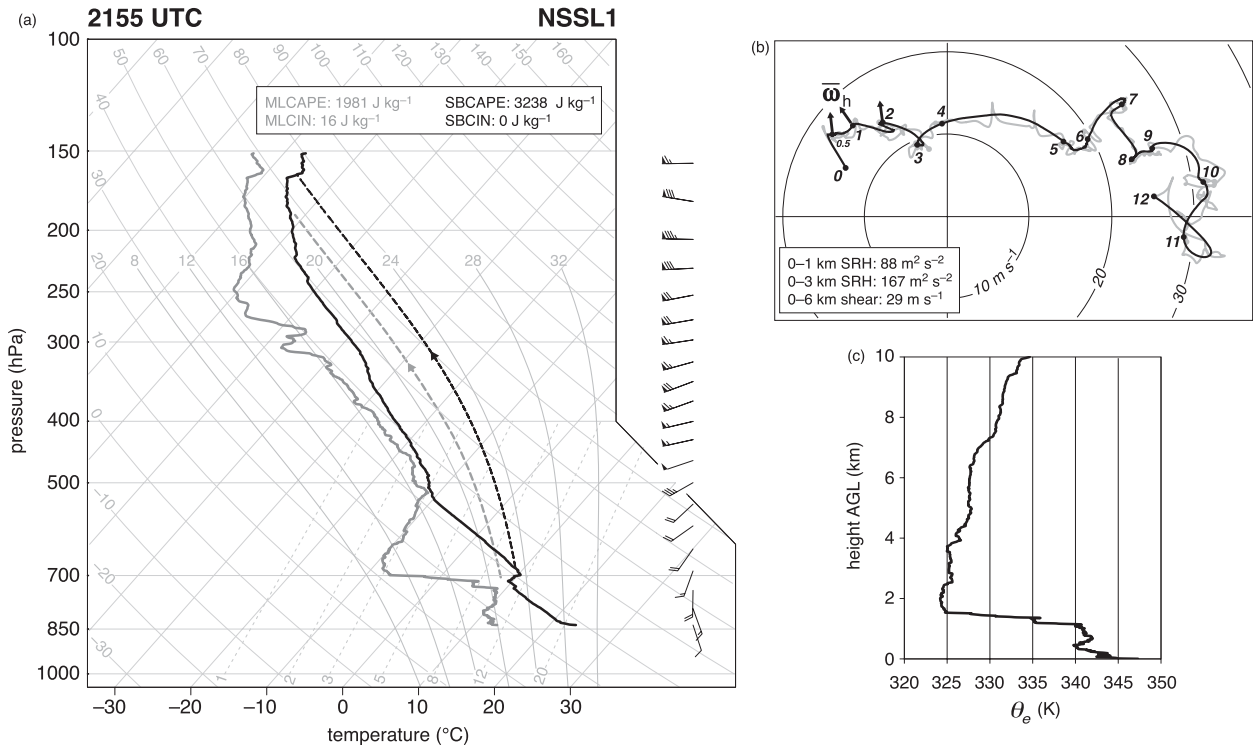


FIG. 2. (a) Skew T - $\log p$ diagram of the 2155 UTC NSSL1 sounding launched southeast of the Goshen County storm. The location of the sounding is shown in Figs. 1 and 4. The wind barbs are ground-relative (half barb = 2.5 m s^{-1} ; full barb = 5 m s^{-1} ; flag = 25 m s^{-1}). Surface-based CAPE and convective inhibition (CIN; SBCAPE and SBCIN, respectively) and mixed-layer CAPE and CIN (MLCAPE and MLCIN, respectively) are indicated for the black and gray parcel process curves, respectively. The CAPE and CIN calculations include the effects of moisture on buoyancy and are based on the pseudoadiabatic ascent of a parcel lifted from the surface (black) or a lifted parcel having the mean potential temperature and water vapor concentration of the lowest 125 mb (gray). (b) Storm-relative hodograph (SRH) derived from the 2155 UTC sounding [a storm motion of $(10.5, -1.3) \text{ m s}^{-1}$ has been subtracted from the ground-relative wind profile]. The black (gray) hodograph is smoothed (unsmoothed); the smoothing was accomplished with a 5-step Leise filter. Numerals along the black hodograph trace indicate heights above ground level in km. The direction of the environmental horizontal vorticity vector ω_h is indicated at 0.5, 1, and 2 km AGL (the environment is assumed to have no mean vertical velocity). The 0–1-km SRH, 0–3-km SRH, and 0–6-km shear vector magnitude are indicated for the smooth hodograph. (c) Vertical profile of pseudoequivalent potential temperature θ_e obtained using Bolton's (1980) formula.

hereafter Part II). Other articles will cover the genesis of the tornado (2148–2202 UTC; Kosiba et al. 2012, manuscript submitted to *Mon. Wea. Rev.*), its mature phase (2202–2212 UTC; J. Wurman et al. 2012, unpublished manuscript) and demise (2212–2230 UTC; Y. Richardson et al. 2012, unpublished manuscript), and analyses of the storm derived from data assimilation into a numerical cloud model (J. Marquis et al. 2012, unpublished manuscript).

The aim of this paper is to use multiplatform observations to document the kinematic and thermodynamic attributes of the Goshen County storm during its pre-tornadic phase. (Our focus in Part II is the dynamics responsible for the increase in low-level rotation after 2142 UTC, as tornadogenesis neared.) Section 2 describes the dataset and analysis techniques. Section 3 deals with the maturation of the supercell (nominally the 2100–2140 UTC period) and is largely based on single-Doppler

observations from the nearest WSR-88D and coarse-resolution dual-Doppler observations obtained by combining the WSR-88D velocity data with data obtained from one of the early-scanning VORTEX2 mobile radars. Section 4 is concerned with the intensification of rotation that occurred after 2140 UTC, which is also the time period within which high-resolution dual-Doppler observations were collected (i.e., observations from a pair of VORTEX2 mobile radars). A discussion and summary of the findings are presented in sections 5 and 6, respectively.

2. Data and analysis techniques

The analysis of the pretornadic phase is based on data collected by the following platforms (Fig. 4): (i) the Cheyenne WSR-88D (KCY5; 60–70 km south-southwest of the mesocyclone, 2100–2148 UTC); (ii) the DOW6 radar,

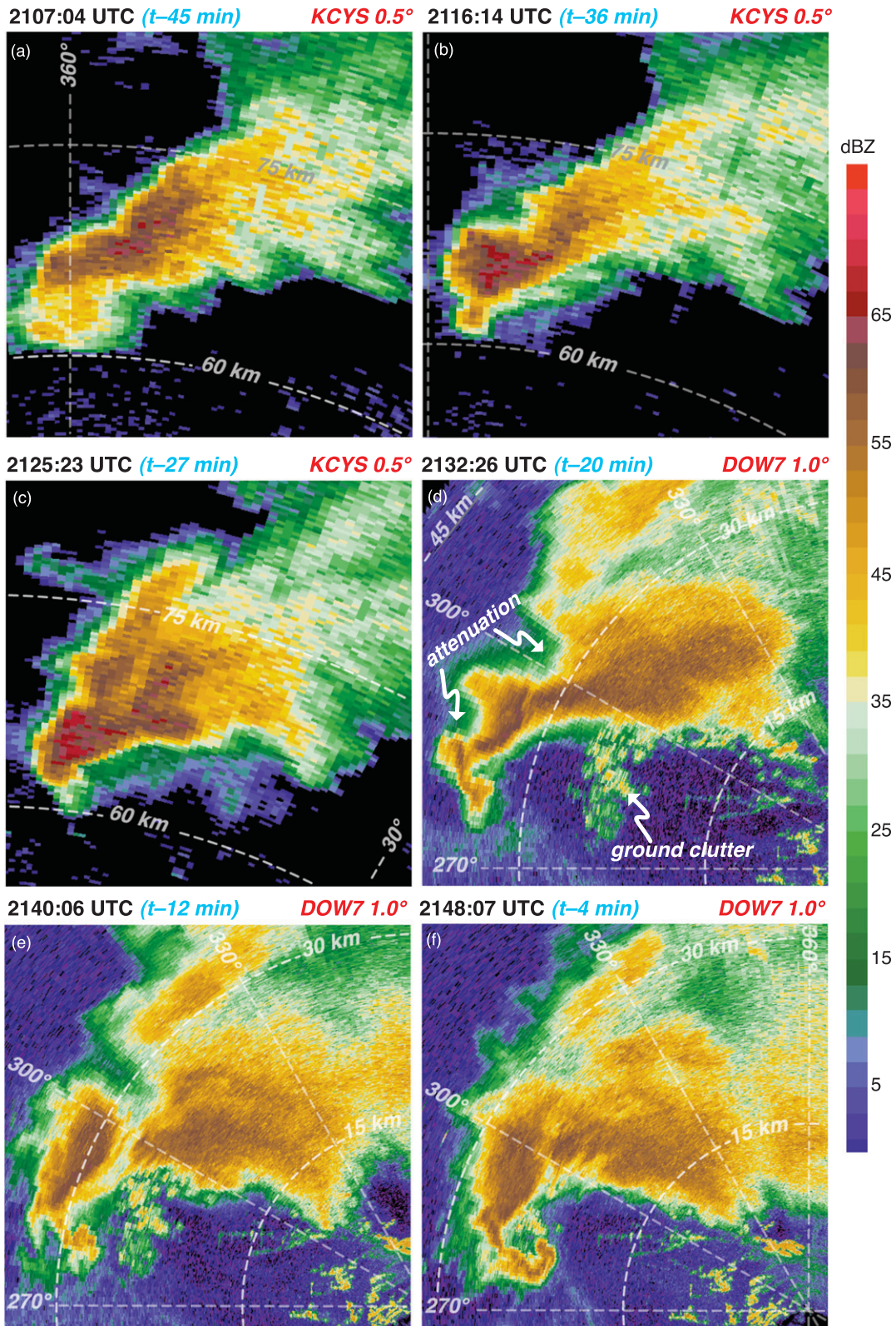


FIG. 3. Unedited logarithmic radar reflectivity factor (dBZ) observed by the KCYS WSR-88D (0.5° elevation angle) and DOW7 radars (1° elevation angle) at (a) 2107:04, (b) 2116:14, (c) 2125:23, (d) 2132:26, (e) 2140:06, and (f) 2148:07 UTC (“ $t - X$ min” indicates X min prior to tornadogenesis). The DOW7 reflectivity is uncalibrated.

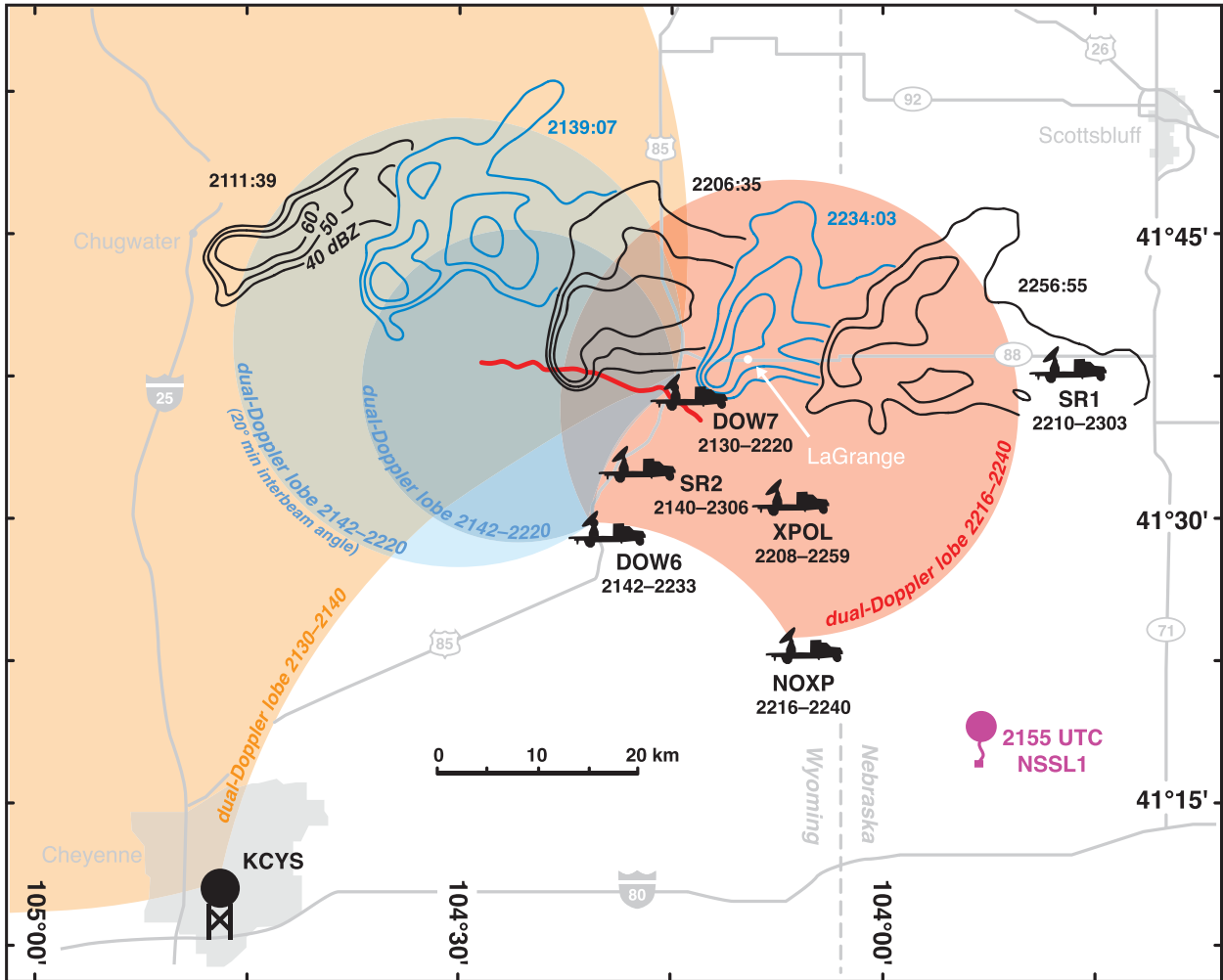


FIG. 4. Large-scale depiction of the track of the Goshen County storm on 5 Jun 2009 as evidenced by the 40-, 50-, and 60-dBZ isopleths of logarithmic reflectivity factor at $z = 2$ km from objectively analyzed KCYS WSR-88D data. The locations of the VORTEX2 storm-scale (SR1 and SR2) and mesocyclone-scale (DOW6, DOW7, NOXP, and XPOL) radars, KCYS WSR-88D, 2155 UTC NSSL1 mobile sounding, tornado track (red line), and select major roads and cities also are indicated. The dual-Doppler lobes used for the 3D wind syntheses presented in this study, and in companion studies focusing on later time periods, are overlaid (based on a 30° minimum interbeam angle, except where noted).

which was deployed at 2142 UTC (approximately 25 km southeast of the mesocyclone, 2142–2148 UTC); (iii) the DOW7 radar, which was deployed at 2130 UTC (25–35 km east-southeast of the mesocyclone, 2130–2148 UTC); and (iv) six National Severe Storms Laboratory (NSSL) mobile mesonet probes (Straka et al. 1996; Waugh and Fredrickson 2010), operating in collaboration with The Pennsylvania State University, which reached the precipitation on the forward flank of the storm at roughly 2140 UTC and obtained wind, pressure, temperature, and relative humidity data at a height of approximately 2 m above ground level (AGL). The analysis techniques applied to the radar and mobile mesonet data are described in sections 2a and 2b, respectively.

a. Objective analysis of radar data and dual-Doppler wind synthesis

Prior to 2130 UTC, analyses rely on single-Doppler radar data from KCYS (Table 1). Three-dimensional (3D) winds are available via dual-Doppler wind retrievals after 2130 UTC. During the 2130–2142 UTC period, analyses rely on long-baseline (69.2 km), dual-Doppler wind retrievals using the KCYS and DOW7 radars (orange dual-Doppler lobes in Fig. 4; the effective resolution is relatively coarse and the data horizon is relatively high given the long baseline). During the 2142–2148 UTC period, short-baseline (15.4 km), dual-Doppler wind retrievals are available from the DOW6–DOW7 pair

TABLE 1. Summary of gridded radar analyses. Analysis times correspond to the time at which volumetric data collection began for a given volume (this was the time at which the radar beam was at its lowest elevation angle of 0.5°). The data horizons are valid at the circulation centers (or, for single-Doppler wind fields, at the location of maximum azimuthal wind shear) identified at $z = 1.5$ km. In the case of dual-Doppler analysis times, the data horizon of the radar farthest from the circulation is given, which is the lowest level at which radar beams overlap.

Analysis time (UTC)	Single (S) or dual (D) Doppler	Radar(s)	κ_0 (km ²)	Baseline (km)	Min allowable interbeam angle	Data horizon at circulation center (km above grid bottom)	Lon (°W)/lat (°N) of grid origin
2111:39	S	KCYS	2.64	—	—	1.1	104.7874/41.6847
2116:14	S	KCYS	2.64	—	—	1.1	104.7528/41.6814
2120:48	S	KCYS	2.64	—	—	1.1	104.7183/41.6781
2125:23	S	KCYS	2.64	—	—	1.1	104.6837/41.6748
2129:58	D	KCYS, DOW7	2.64	69.2	30°	1.1	104.6491/41.6714
2134:33	D	KCYS, DOW7	2.64	69.2	30°	1.1	104.6145/41.6681
2139:07	D	KCYS, DOW7	2.64	69.2	30°	1.1	104.5800/41.6648
2142:00	D	DOW6, DOW7	0.48, 2.64	15.4	20°	0.2	104.5582/41.6627
2144:00	D	DOW6, DOW7	0.48, 2.64	15.4	20°	0.2	104.5431/41.6613
2146:00	D	DOW6, DOW7	0.48, 2.64	15.4	20°	0.2	104.5280/41.6598
2148:00	D	DOW6, DOW7	0.48, 2.64	15.4	20°	0.2	104.5129/41.6584

(blue dual-Doppler lobes in Fig. 4; the shorter baseline affords a finer spatial resolution and lower data horizon than the KCYS–DOW7 pair provides).

KCYS scanned 14 elevation angles (0.5° – 19.5°) approximately every 5 min. DOW6 and DOW7 collected synchronized volumes comprising 12 elevation angles (0.5° – 16.0°) every 2 min. Edited radar data (ground clutter was removed and aliased velocities were dealiased during editing) were objectively analyzed to a $40 \text{ km} \times 40 \text{ km} \times 10 \text{ km}$ Cartesian grid having a 0.25-km grid spacing using the two-pass Barnes successive corrections method (Barnes 1964; Koch et al. 1983; Majcen et al. 2008). The amount of smoothing was determined by a conservative estimate of the data spacing d in the region of the storm that was scanned.

In dual-Doppler observation periods, d was dictated by what could be resolved by the radar *farthest* from the storm. For the period of single-Doppler observations by KCYS (pre-2130 UTC), as well as for the period of dual-Doppler observations by the KCYS–DOW7 pair (2130–2142 UTC), d was determined by the resolution of KCYS. The angular data spacing was 0.5° in azimuth (approximately half the beamwidth of the WSR-88D; i.e., there was oversampling in azimuth) and 0.4° – 3.9° in elevation. For 1° angular data spacing at a range of 70 km, $d = 1.22 \text{ km}$ (a 1° angular data spacing, which is the elevation angle spacing at roughly 6 km AGL at a range of 70 km, seemed like a good compromise). For the period of dual-Doppler observations by the DOW6–DOW7 pair (2142–2148 UTC), the coarsest angular data spacing was 1° (in elevation) and the most distant parts of the storm of relevance in this study were as far as 30 km from the radars (DOW6 and DOW7 were approximately equidistant from the storm during this period; Fig. 4). This yields $d = 0.52 \text{ km}$.

The Barnes weight function was isotropic. The smoothing parameter on the first pass, κ_0 , was chosen based on the recommendation of Pauley and Wu (1990), who suggested a value of $(1.33d)^2$. On the second pass, $\kappa = 0.3\kappa_0$, in light of the findings of Majcen et al. (2008). For the objective analyses of the KCYS data, as well as for the objective analyses of the DOW7 data that were combined with the KCYS data for the dual-Doppler analyses in the 2130–2142 UTC period, κ_0 was set to $(1.33 \text{ km} \times 1.22 \text{ km})^2 = 2.64 \text{ km}^2$. For the objective analyses of the DOW6 and DOW7 data used for dual-Doppler syntheses in the 2142–2148 UTC period, κ_0 was set to $(1.33 \text{ km} \times 0.52 \text{ km})^2 = 0.48 \text{ km}^2$. The DOW6 and DOW7 data in the 2142–2148 UTC period also were objectively analyzed using the larger κ_0 (2.64 km^2) in order to produce a set of analyses that could be more fairly compared with analyses prior to 2142 UTC. Hereafter, analyses derived using $\kappa_0 = 2.64 \text{ km}^2$ ($\kappa_0 = 0.48 \text{ km}^2$) are referred to as *smooth* (*fine*) analyses. In subsequent sections, figure captions will clearly indicate which grids were used. The theoretical two-pass response curves for the smooth and fine objective analyses are displayed in Fig. 5.

The analysis times, objective analysis parameters, and latitudes and longitudes of the grid origins are tabulated in Table 1. The grids extend from -10 to 30 km in the x and y directions. The bottom of the grid is at 1.610 km MSL at each analysis time, which is roughly the mean elevation at the location of the midlevel mesocyclone in the dual-Doppler window (2130–2148 UTC). The DOW6, DOW7, and KCYS radars were at 1.565 , 1.485 , and 1.852 km above mean sea level (MSL), respectively (hereafter, all altitudes are with respect to the bottom of the grid). The grid was translated at a velocity $(10.45, -1.34 \text{ m s}^{-1})$ equal to the mean velocity of the

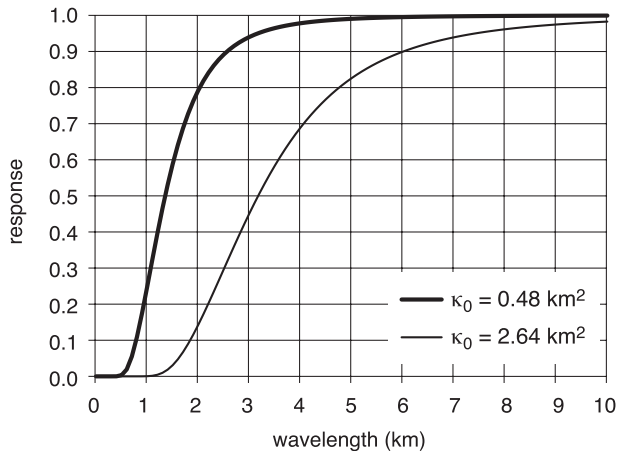


FIG. 5. Theoretical Barnes filter response functions for a two-pass filter with smoothing parameters $\kappa_0 = 2.64 \text{ km}^2$ (thin curve) and $\kappa_0 = 0.48 \text{ km}^2$ (thick curve) on the first pass. On the second pass, the smoothing parameters are reduced to 30% of the first-pass values.

dual-Doppler-based circulation center (using the aforementioned smooth analyses) at $z = 1.5 \text{ km}$ from 2130 to 2148 UTC. The grid was translated in order to minimize the grid-relative motion of the storm, which mitigates time-interpolation errors in the trajectory calculations that are relied upon in section 4 and Part II.

The maximum allowable distance between an observation and a grid point was $(5\kappa_0)^{1/2}$, or 3.6 (1.5) km for grids used for the smooth (fine) dual-Doppler wind syntheses. The extrapolation of data was not permitted in the objective analyses; radar data only were interpolated to grid points within the data region. The motion of the mesocyclone during the time taken to collect a volume of data was accounted for during the gridding process by correcting the horizontal position of each datum by the distance traveled by the storm between the datum collection time and the analysis time. This prevents an artificial tilt with height of storm features owing to their motion between consecutive radar sweeps.

The gridding procedure was necessarily iterative: (i) raw data were interpolated to the translating grid using an estimated motion; (ii) the three-dimensional wind field was retrieved (via the method to be described below); (iii) the circulation center at $z = 1.5 \text{ km}$ was identified;² (iv) the mean motion of the circulation

center in the 2130–2148 UTC period was used to refine the translation velocity and grid origins at each analysis time; and (v) the raw data were reinterpolated to the new grids using the updated translation velocity. For simplicity, a constant grid translation velocity was used. The circulation center at $z = 1.5 \text{ km}$ is located at the grid origin at 2130 and 2148 UTC, but at intermediate times (depending on how much the storm motion near the analysis time deviated from the longer-term mean motion) and altitudes above or below $z = 1.5 \text{ km}$ (depending on the tilt of the circulation), the circulation center may not coincide with the origin (the displacement is usually no more than 1 km).³

The three-dimensional wind field was synthesized from the gridded radial velocity fields using an upward integration of the anelastic mass continuity equation, with the lower boundary condition being that vertical velocity w vanishes there (i.e., $w = 0$ at $z = 0$). The zonal u , meridional v , and vertical velocity fields were iteratively adjusted (Brandes 1977; Dowell and Shapiro 2003) until the change in $\bar{\rho}w$ (where $\bar{\rho}$ is the reference density at a given height) between iterations was $< 0.01 \text{ kg m}^{-2} \text{ s}^{-1}$ [the wind syntheses were converged for practical purposes at this point; changing the convergence criterion to $0.0001 \text{ kg m}^{-2} \text{ s}^{-1}$ changed the retrieved wind components only by $O(10^{-4} \text{ m s}^{-1})$]. The coefficients in the dual-Doppler equations that involve direction cosines and radial velocities [e.g., Ray et al. 1980, their Eq. (5)] were extrapolated downward to grid points located below the lowest elevation angle scanned (0.5°) in order to apply the lower boundary condition. The missing near-surface coefficients were set to be equal to those at the lowest level at which both radars collected data. The downward extrapolation was minimal for the DOW6–DOW7 dual-Doppler wind syntheses because the lowest grid level having intersecting beams was only one grid level (0.25 km) above the grid bottom. (The extrapolation was only done in order to integrate the continuity equation; any extrapolated wind components were reset to “missing” after a wind synthesis was completed.) The downward extrapolation for the KCYS–DOW7 wind syntheses was 1.25 km, however. Experimental wind syntheses in the 2142–2148 UTC period using

² Circulation centers were identified at the location of the minimum in the field of Okubo–Weiss number (W ; Okubo 1970; Weiss 1991) following Markowski et al. (2011). The W field was further smoothed in order to filter submesocyclone-scale features. Scales smaller than 2 km were filtered using a three-step Leise (1982) filter, which suppresses wavelengths $\leq 8\Delta$, where Δ is the grid spacing.

³ Although the mean motion was faster and less rightward in the 2100–2130 UTC period, the grid to which raw radar observations from this period were interpolated was translated at the same constant velocity as in the 2130–2148 UTC period. Given that the main reason for using a translating grid was to reduce time interpolation errors in the trajectory calculations, we were not concerned with a grid-relative drift of the storm during the single-Doppler observation period.

the DOW6–DOW7 radar pair (low data horizon), but with the radial velocity data below $z = 1.25$ km being set to missing in order to emulate the wind data relied upon for the KCYS–DOW7 dual-Doppler wind syntheses prior to 2142 UTC (high data horizon), have vertical velocity fields that are qualitatively similar to the syntheses incorporating the full volumes of radial velocity data. The differences in maximum vertical velocity between the two sets of vertical velocity fields are less than 10%. The qualitative characteristics of vertical velocity isosurfaces and vortex lines (to be described in subsequent sections) also are insensitive to the degree of downward extrapolation.

Finally, the effect of hydrometeor fall speeds on the radial velocities was neglected because of the relatively small antenna elevation angles used (most of the winds in the domain of interest were retrieved from radial velocity data obtained from scans having elevation angles less than 10°). Furthermore, a parameterization of precipitation fall speed from reflectivity would have been problematic for this case because of uncalibrated DOW reflectivity factors, the potential for Mie scattering in the regions of highest reflectivity (the DOW wavelength is 3 cm), and attenuation in heavy precipitation. Comparisons of wind syntheses in which fall speeds were parameterized in terms of the maximum reflectivity observed by the two radars at a grid point yielded only small differences [$O(10^{-2} \text{ m s}^{-1})$ rmse for the wind components at $z = 0.75$ km; $O(10^{-1} \text{ m s}^{-1})$ rmse in a volume extending from $z = 0.25$ km to $z = 3.0$ km]; thus, we are confident that the neglect of fall speeds does not change any qualitative interpretation of the results.

b. Surface analyses derived from mobile mesonet data

The mobile mesonet data presented in this article were obtained from the probes originally developed by Straka et al. (1996) and modified by Waugh and Fredrickson (2010). Time, latitude, longitude, temperature, relative humidity, pressure, and wind velocity were recorded at 1-s intervals by instrument systems aboard six vehicles. Temperature and relative humidity data collected while a vehicle was stationary were omitted because of concerns about insufficient aspiration of the probes. Although wind data were not used for any quantitative calculations (e.g., divergence), wind data obtained during periods of significant vehicle acceleration also were excluded from analyses (the maximum allowed 1-Hz variation in vehicle speed and direction were 2 m s^{-1} and 2° , respectively). Instrument specifications, error analyses, and a more detailed description of

the quality control techniques have been described by Straka et al. (1996), Markowski et al. (2002), and Waugh and Fredrickson (2010).

High-frequency noise in the raw data was suppressed using two passes of a triangular weighting function with a filter radius of 10 s. The spatial scales retained by such filtering depend on vehicle speed, but for typical vehicle speeds during data collection (20 – 25 m s^{-1}), this filtering significantly damped features having wavelengths less than 0.3 km. Surface analyses were produced from time-to-space-converted smoothed observations following Markowski et al. (2002) and Shabbott and Markowski (2006). Given the relatively small number of probes, 10 min of data were used to construct each analysis (relatively large windows of observations were required to achieve sufficient data coverage in order to construct meaningful analyses). Our analyses admittedly make an ambitious assumption about the steadiness of the storm; however, we note that similarly long steady-state assumptions have been employed in many past pseudo-dual-Doppler analyses. In manually contouring mobile mesonet-derived fields, we subjectively gave more weight to observations closest to the reference time of the analysis. All analyses overlay the raw observations so that the reader may assess the credibility of the analyses.

3. Supercell maturation: 2100–2140 UTC

Reflectivities observed by KCYS at most elevations steadily increased in the storm during the 2100–2130 UTC period (Figs. 3a–c). Isosurfaces of azimuthal wind shear⁴ reveal that the regions of significant cyclonic and anticyclonic shear spanned a significant depth of the storm (>7 km) even as early as the 2111 UTC analysis time (Fig. 6). In this early stage of the storm, the isosurfaces of significant cyclonic and anticyclonic shear have a structure and alignment that is consistent with the tilting of environmental vortex lines by an updraft envisioned by Davies-Jones (1984), among others (Fig. 6a). A deep mesocyclone (mesoanticyclone) is present south of (within) the precipitation region of the storm, where later dual-Doppler wind syntheses reveal updraft (downdraft).

Even though we could not retrieve vertical vorticity during this early period of single-Doppler observations, we refer to the regions of significant midlevel

⁴ The azimuthal wind shear is defined as $r^{-1}\partial v_R/\partial\phi$, where r is the range from the radar, v_R is the radial velocity, and ϕ is the radar azimuth (not to be confused with the mathematical coordinate).

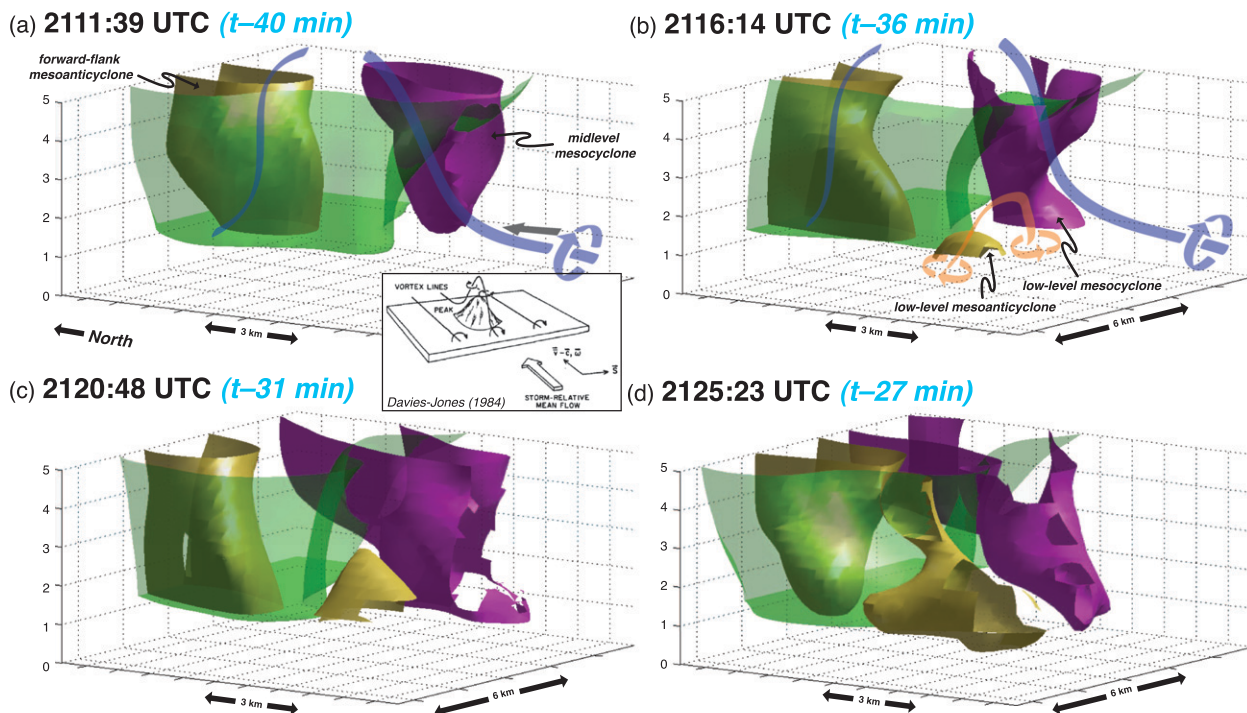


FIG. 6. Three-dimensional presentation of the objectively analyzed 0.005 s^{-1} azimuthal shear isosurface (purple), -0.005 s^{-1} azimuthal shear isosurface (yellow), and 40-dBZ logarithmic reflectivity factor isosurface (green) at (a) 2111:39, (b) 2116:14, (c) 2120:48, and (d) 2125:23 UTC as observed by the KCYS WSR-88D. Axis labels are in km. Some hypothetical vortex lines also have been added in (a) and (b) that are at least plausible given the 3D azimuthal shear fields. The blue vortex lines in (a) and (b) pass through the midlevel cyclonic and anticyclonic azimuthal shear maxima and are intended to represent environmental vortex lines; the orange vortex line in (b) is associated with the couplet of negative and positive azimuthal shear that develops in the RFD region, straddling the hook echo. The broad gray arrow in (a) indicates the direction of the observed mean storm-relative wind at low levels. The inset in (a) is a schematic from Davies-Jones (1984) showing what happens when an environmental vortex line aligned with the storm-relative wind (i.e., the environmental vorticity is streamwise) is lifted, with the displacement represented by an isentropic hill.

cyclonic (anticyclonic) azimuthal shear as mesocyclones (mesoanticyclones) because the vertical vorticity isosurfaces constructed from the dual-Doppler observations after 2130 UTC (to be discussed later in this section) were practically identical in appearance. Furthermore, hypothetical vortex lines have been added to Figs. 6a and 6b that are plausible given the three-dimensional azimuthal shear fields. The vortex line calculations enabled by the post-2130 UTC dual-Doppler observations (also to be discussed later in this section) reveal actual vortex lines at the later times that are similar to the vortex lines we have inferred during the single-Doppler observation period. Our motivation for attempting to infer the three-dimensional vorticity field during the single-Doppler observation period is that we wish to provide circumstantial evidence for the presence of baroclinically altered vortex lines (see next paragraph) at a relatively early stage in storm development. High-resolution dual-Doppler observations of supercells at such an early stage are rare in general.

By 2116 UTC, azimuthal shear isosurfaces (Fig. 6b) suggest the upward development of a couplet of low-level, counter-rotating vortices straddling the developing hook echo (Fig. 3b). This evolution suggests the likely presence of new vortex lines arching upward out of the outflow on the rear flank of the storm (note the orange line in Fig. 6b), an interpretation that will be confirmed by actual vortex lines constructed in the dual-Doppler observation period. The arching vortex lines inferred at 2111 UTC (the blue vortex lines in Fig. 6a) are aligned with the low-level environmental vorticity (Fig. 2b), whereas the low-level arching vortex lines inferred at 2116 UTC (the orange vortex lines in Fig. 6b) are at roughly a right angle to the former, with an alignment roughly parallel to the orientation of the trailing rear-flank gust front (i.e., west-east). Further discussion of vortex lines is deferred to the period of dual-Doppler observations.

The maximum (cyclonic) azimuthal wind shear at midlevels (nominally $z = 4 \text{ km}$) gradually increased throughout the 2100–2140 UTC period (dark green

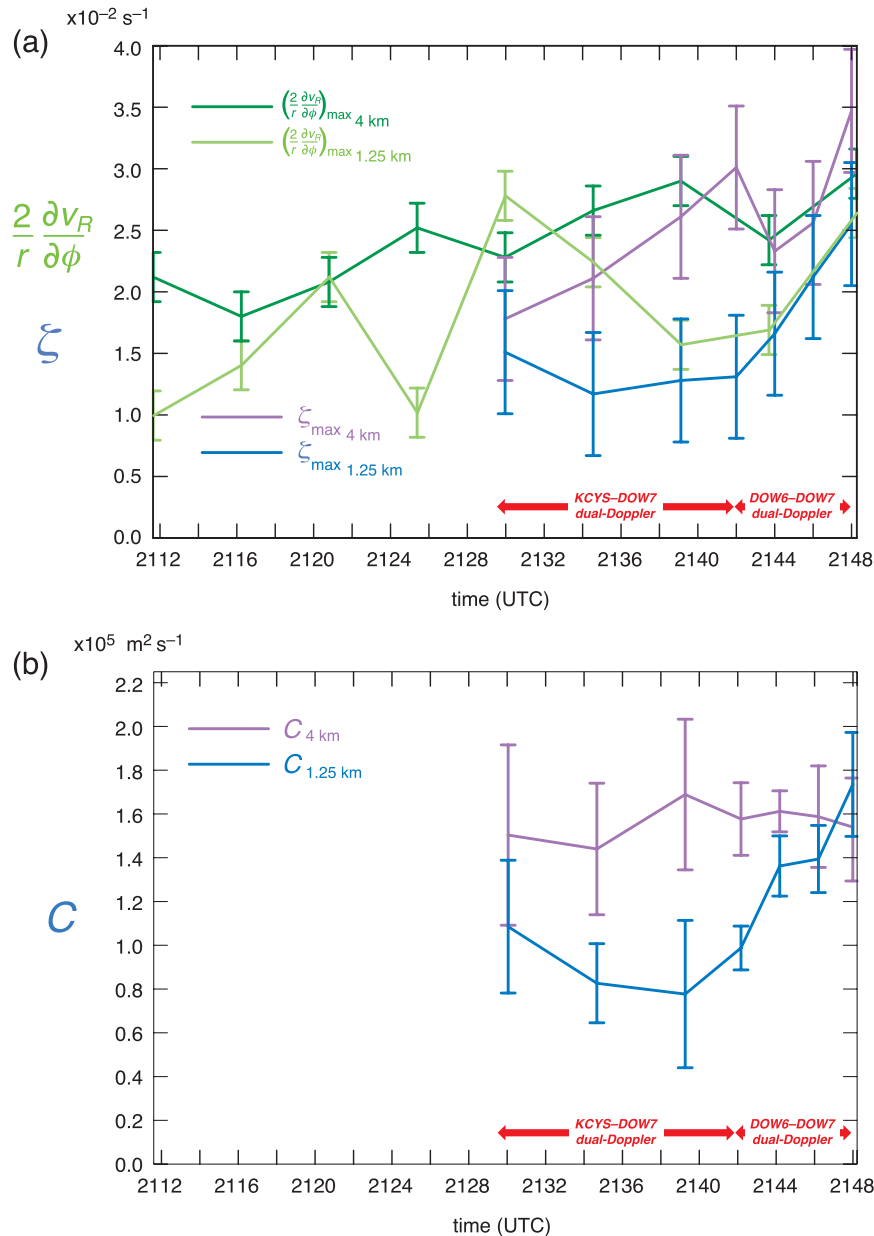


FIG. 7. (a) Time series of the maximum azimuthal shear times 2 observed by KCYS, $2r^{-1}(\partial v_R/\partial \phi)_{\max}$ (2 times the azimuthal shear is equal to the vertical vorticity in the core of a Rankine vortex), and maximum vertical vorticity, ζ_{\max} , derived from the smooth ($\kappa_0 = 2.64 \text{ km}^2$) dual-Doppler wind syntheses (KCYS and DOW7 from 2130 to 2142 UTC; DOW6 and DOW7 from 2142 to 2148 UTC). Times series are shown at $z = 1.25$ and 4 km (see legend). The 1.25-km altitude is the lowest altitude at which dual-Doppler winds exist in the KCYS-DOW7 radar pair. The error bars indicate estimated uncertainties based on the assumption of 1 m s^{-1} uncertainty in the objectively analyzed radial velocity and retrieved horizontal wind components. (b) As in (a), but for circulation about a 2-km-radius circle centered on the circulation at $z = 1.25$ and 4 km. The circulation center was identified as the location of the minimum in the smoothed field of Okubo-Weiss number (W). The uncertainties were estimated as the standard deviations of the circulations obtained with respect to 1000 randomly perturbed circulation centers (the uncertainty in C due to random u and v errors is negligible compared with the uncertainty in C due to the uncertainty in the location of the circulation center). The standard deviation of the distances between the randomly perturbed circulation centers and the circulation center identified from the W field is 1.0 km (0.5 km) in the 2130–2140 UTC (2142–2148 UTC) period, which we estimate as the uncertainty in the location of the circulation center.

trace in Fig. 7a), which we interpret as a gradual strengthening of the midlevel mesocyclone. The dual-Doppler analyses, the first of which is available at 2129 UTC, reveal a similar upward trend in maximum midlevel vertical vorticity (purple trace in Fig. 7a). Moreover, the midlevel vertical vorticity has a magnitude comparable to 2 times the magnitude of the maximum midlevel ($z = 4$ km) azimuthal wind shear, which is consistent with nearly solid-body rotation around a circulation center at the vorticity maximum. Circulation, $C = \oint \mathbf{v} \cdot d\mathbf{l}$, where \mathbf{v} is the three-dimensional velocity and $d\mathbf{l}$ is an element of the circuit along which the integration is performed, in a counterclockwise direction), computed about a 2-km-radius circle centered on the midlevel circulation, is approximately constant in the 2130–2140 UTC period (purple trace in Fig. 7b).

The time series of maximum azimuthal wind shear at low levels (nominally $z = 1.25$ km) has no obvious trend in the 2100–2140 UTC period (light green trace in Fig. 7a),⁵ and the time series of maximum low-level vertical vorticity available from the post 2130 UTC dual-Doppler observations indicates a fairly steady low-level mesocyclone through 2140 UTC as well (blue trace in Fig. 7a; also see Figs. 8a–c). Circulation at 1.25 km exhibits perhaps a slight downward trend during the same time period (blue trace in Fig. 7b), but confidence in this trend is low given the uncertainty in the C calculations (per the error bars in Fig. 7b).

Figure 8 displays dual-Doppler-derived storm-relative wind vectors, vertical vorticity, and regions of significant horizontal convergence at $z = 1.25$ km during the 2130–2148 UTC period using the smooth ($\kappa_0 = 2.64 \text{ km}^2$) wind syntheses. The amount of smoothing is constant throughout the period (and was dictated by what the most distant radar, KCYS, could resolve) so that trends in scale-dependent kinematic quantities (e.g., vorticity and convergence) can be interpreted fairly (Trapp and Doswell 2000). In the 2130–2140 UTC period (Figs. 8a–c), we note the following: (i) the cyclonic and anticyclonic vertical vorticity extrema

⁵ The time series of maximum azimuthal shear at low levels also is much noisier than at midlevels. One possibility is that the smaller scale of the low-level mesocyclone, relative to the midlevel mesocyclone, makes its intensity more dependent on the location of the radar beams relative to the axis of rotation. The relatively noisy time series of maximum low-level azimuthal shear also could be attributable to the influence of the gust front. Azimuthal shear can be associated with deformation or rotation. Given that gust fronts can be associated with significant deformation and rotation, whereas mesocyclones are dominated by rotation, one might expect low-level azimuthal shear to be intrinsically more variable in time than midlevel shear.

coincide with the azimuthal shear extrema identified in the single-Doppler observation period; (ii) the maximum vertical vorticity is roughly steady, consistent with the time series in Fig. 7a; (iii) the updraft region, implied by the region of strong horizontal convergence, is within cyclonic vertical vorticity on average, which is consistent with the tilting of environmental vorticity having a significant streamwise component; and (iv) the updraft region is “bowed” in the vicinity of the hook echo, as commonly has been observed (e.g., Lemon and Doswell 1979), and has a low-altitude eastward extension along the forward-flank echo, which seems to coincide with a cloud feature known to storm chasers as a *beaver’s tail* (Fig. 9a).

Isosurfaces of significant vertical vorticity ($>0.01 \text{ s}^{-1}$ in magnitude) at the 2129 UTC analysis time depict a low-level and midlevel mesocyclone that are spatially separated (Fig. 10a). The midlevel vertical vorticity maximum lies approximately 4 km northeast of the low-level maximum. Vortex lines integrated from the midlevel vertical vorticity maximum originate in the environment to the south (dark blue lines in Fig. 10a)⁶—that is, the environmental vortex lines point toward the north, which is consistent with the environmental wind profile sampled by mobile soundings (Fig. 2b). The other ends of the vortex lines exit the top of the data region. In contrast, the vortex lines that surround the circulation center at $z = 1.5$ km form arches that join the low-level cyclonic and anticyclonic vertical vorticity extrema that straddle the hook echo and rear-flank downdraft (RFD) behind the gust front (black lines in Fig. 10a). The low-level vortex line arches are similar to those documented by Straka et al. (2007) in the Dimmitt, Texas, tornadic supercell observed in VORTEX1, Markowski et al. (2008) in other VORTEX1 storms (both tornadic and nontornadic; note especially

⁶ Vortex lines were computed using a fourth-order Runge–Kutta algorithm. Velocity derivatives were computed using fourth-order, centered differences, except near data boundaries where second-order, uncentered differences were used. The qualitative characteristics of the vortex lines are robust for reasonable ranges of smoothing [e.g., see the appendix in Markowski et al. (2008)]. Vortex-line calculations originating within the midlevel mesocyclone (e.g., the blue lines in Fig. 10) are qualitatively insensitive to the observed variations in the magnitude of the horizontal gradient of vertical velocity, $|\nabla_h w|$, within the midlevel mesocyclone [vortex lines were computed from additional locations within the midlevel mesocyclone (not shown) spanning a wide range of $|\nabla_h w|$], which suggests that the vortex lines computed from the fixed lattices of points in the midlevel mesocyclone also are qualitatively insensitive to the $|\nabla_h w|$ errors (errors in the retrieved w , which can be large at midlevels, potentially could be accompanied by significant errors in $|\nabla_h w|$).

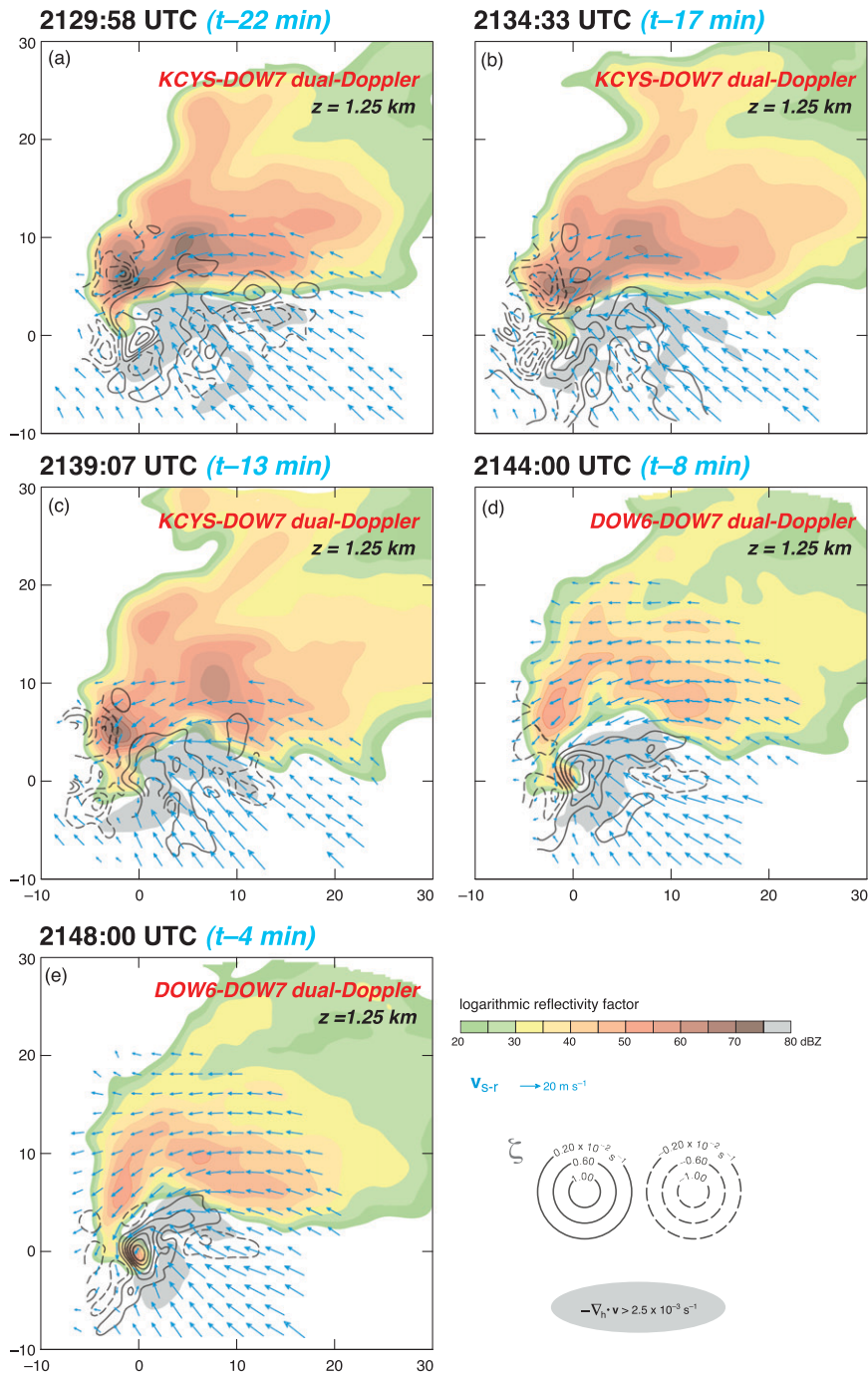


FIG. 8. Vertical vorticity (ζ ; dark gray contours) at $z = 1.25$ km obtained from the smooth ($\kappa_0 = 2.64 \text{ km}^2$) dual-Doppler wind syntheses at (a) 2129:58, (b) 2134:33, (c) 2139:07, (d) 2144:00, and (e) 2148:00 UTC. Storm-relative wind vectors (\mathbf{v}_{S-R}) are plotted at every eighth grid point at the same altitude using blue arrows. Light gray shading indicates where horizontal convergence ($-\nabla_h \cdot \mathbf{v}$) exceeds $2.5 \times 10^{-3} \text{ s}^{-1}$. The wind syntheses in (a)–(c) are derived from the KCYS and DOW7 radars. The syntheses in (d) and (e) are derived from the DOW6 and DOW7 radars. Logarithmic reflectivity factor (color shading) is from KCYS in (a)–(c) and from DOW6 in (d) and (e); the reflectivity fields are at $z = 2$ km [this allows the northeasternmost portion of the echo observed by the KCYS radar to be plotted in (a)–(c)]. Axis labels are in km. The DOW6 reflectivity is uncalibrated. Given the long range from KCYS, 1.25 km is the lowest grid level at which nonextrapolated dual-Doppler-derived wind fields are available throughout most of the storm prior to 2142 UTC (see Table 1), when DOW6 began scanning.

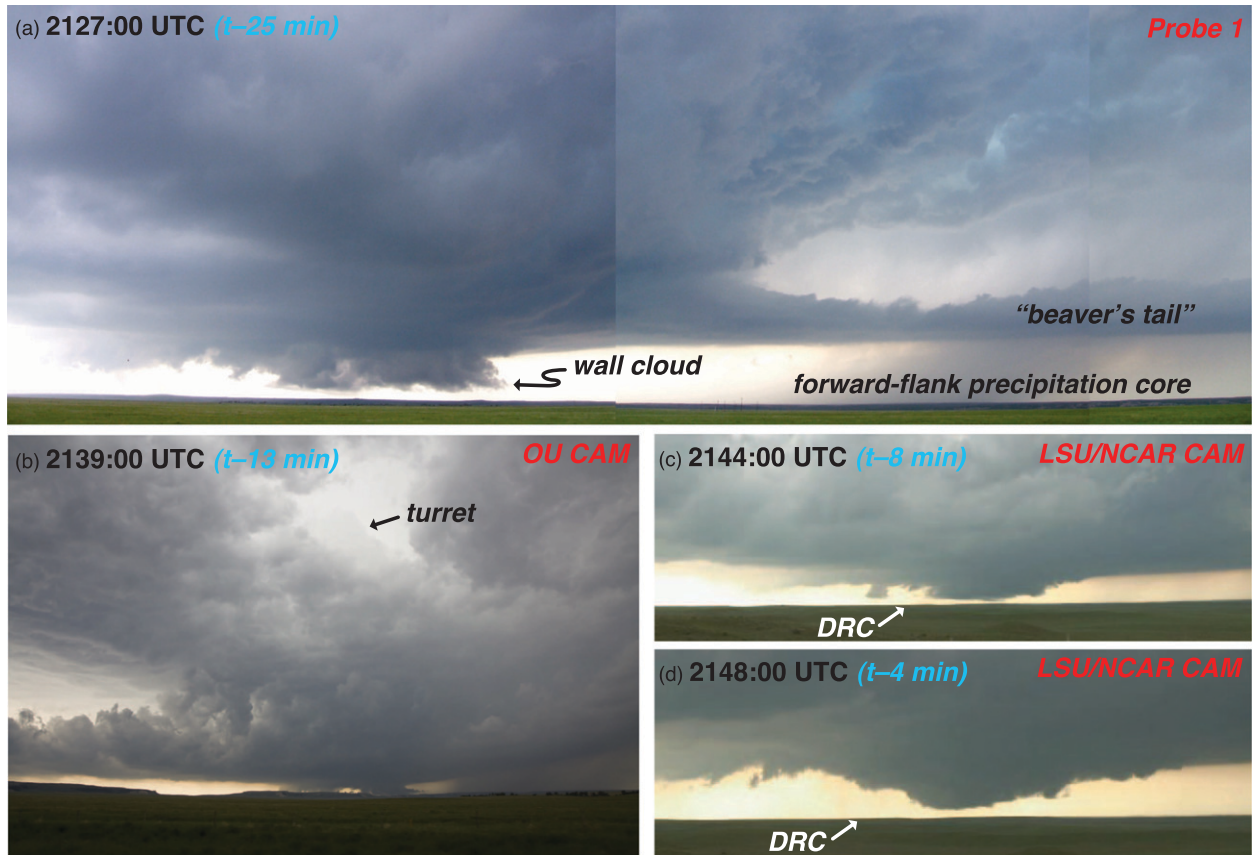


FIG. 9. Photographs and video frames of the Goshen County storm from the east and east-southeast at (a) 2127, (b) 2139, (c) 2144, and (d) 2148 UTC. The photograph in (a) was taken by P. Markowski approximately 20 km east of the wall cloud from a mobile mesonet probe (“Probe 1”). The photograph in (b) was taken by J. LaDue (University of Oklahoma photogrammetry team) from approximately 25 km east of the updraft. The video frames in (c) and (d) are courtesy of N. Atkins and R. Wakimoto (Lyndon State College/NCAR photogrammetry team) and were obtained from the location of DOW7 (the location of DOW7 is indicated in Fig. 4). The location of the DRC observed by the radars at 2144 and 2148 UTC period is indicated in (c) and (d).

the similarity with their Fig. 19), Markowski et al. (2011) and Marquis et al. (2012) in Radar Observations of Thunderstorms and Tornadoes Experiment (ROTATE) storms, and in idealized numerical simulations by Straka et al. (2007), Markowski and Richardson (2008), and Markowski et al. (2010). Some vortex lines (additional select vortex lines are drawn in Fig. 10a using an orange stroke) can be traced into the forward-flank downdraft (FFD) region. The arching vortex lines and their neighbors within the outflow are approximately parallel to the rear-flank gust front and point toward the west. These vortex lines are likely the result of baroclinic vorticity generation, assuming that isopycnics would be approximately parallel to the gust front with higher density to the north, and given that the environmental vorticity in the 0.3–2-km layer points essentially northward (Fig. 2b).

At 2139 UTC, the vortex line structure is similar, but the isosurface associated with the low-level cyclonic

vertical vorticity maximum has grown upward and into the isosurface associated with the midlevel cyclonic vorticity maximum (Fig. 10b); that is, by this time, the mesocyclone region, as depicted by the 0.01 s^{-1} isosurface, has evolved into a deep column of cyclonic rotation spanning the entire depth of the data region. In the ensuing period from 2140 to 2148 UTC, low-level rotation increased dramatically (Figs. 7 and 8d,e). The evolution of this period is analyzed in section 4.

4. The descending reflectivity core and intensification of low-level rotation: 2140–2148 UTC

a. Evolution of the kinematic and reflectivity fields

Both vertical vorticity and circulation (about a 2-km-radius ring centered on the axis of rotation) increased dramatically—roughly doubled—at low levels (i.e., in the lowest $\sim 1.5 \text{ km}$) in the 2140–2148 UTC period

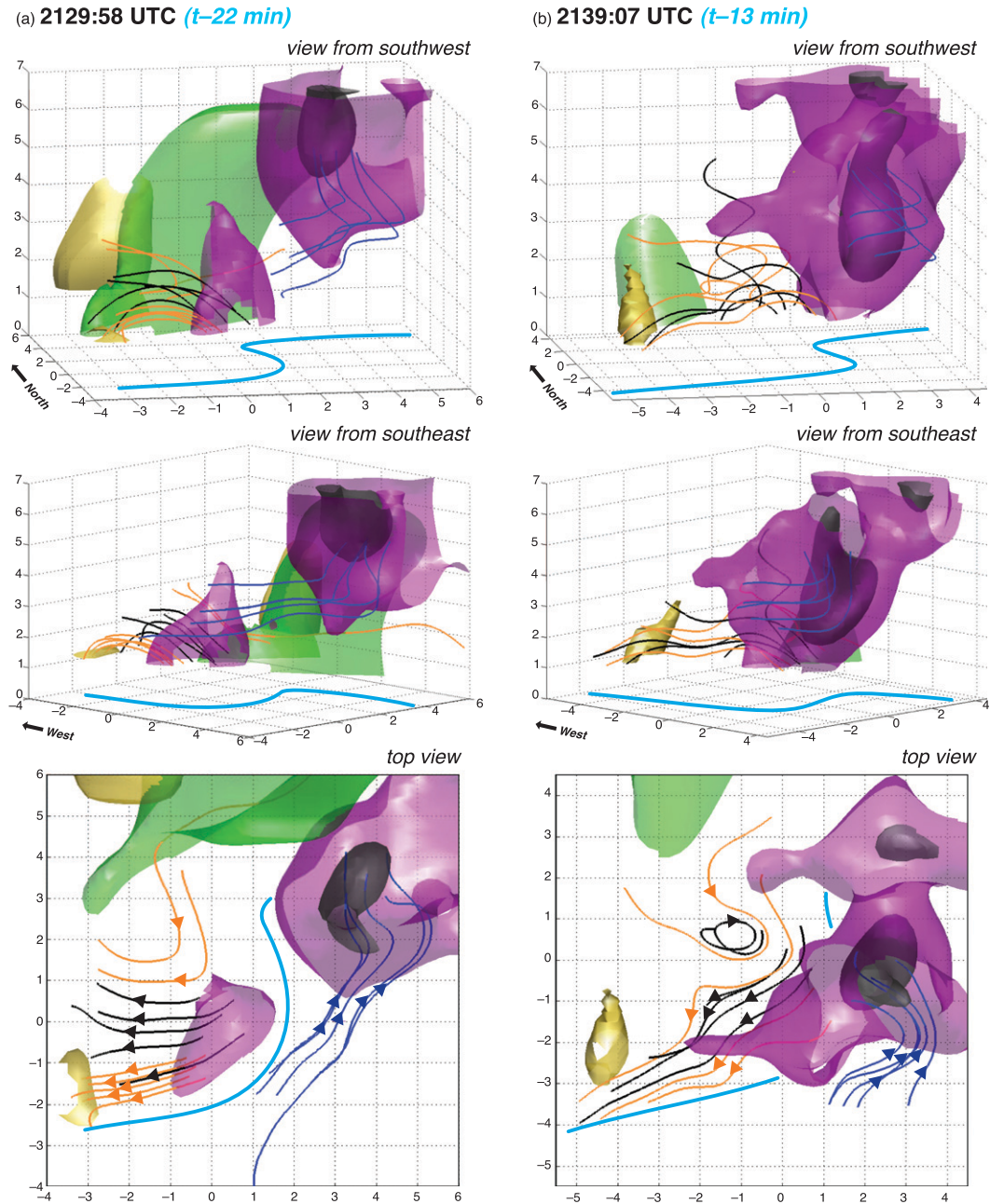


FIG. 10. Various 3D perspectives of the 55-dBZ DOW7 reflectivity isosurface (green) and vertical vorticity isosurfaces of 0.02 s^{-1} (gray), 0.01 s^{-1} (purple), and -0.01 s^{-1} (yellow) at (a) 2129:58 and (b) 2139:07 UTC. Gust fronts are indicated with heavy cyan lines. Vortex lines that pass through the midlevel mesocyclone are blue. These lines pass through a lattice of five points centered on the vertical vorticity maximum at $z = 5 \text{ km}$, with one line passing through the maximum, and the other four lines passing through points that form a $1 \text{ km} \times 1 \text{ km}$ square centered on the maximum. Vortex lines that pass through the low-level mesocyclone are black. These lines pass through a lattice of points at $z = 1.5 \text{ km}$ identical to the lattice at $z = 5 \text{ km}$, centered at the origin. Additional select vortex lines that pass through points in the vicinity of the low-level mesocyclone are orange. The vorticity field is derived from the smooth ($\kappa_0 = 2.64 \text{ km}^2$) dual-Doppler wind syntheses. In the view from above, the direction of the vorticity vector is indicated by the arrowheads. Both the 50- and 55-dBZ reflectivity isosurfaces are shown in Fig. 12, but the 50-dBZ isosurface is suppressed above in order to improve the visibility of the other isosurfaces and vortex lines. Axis labels are in km.

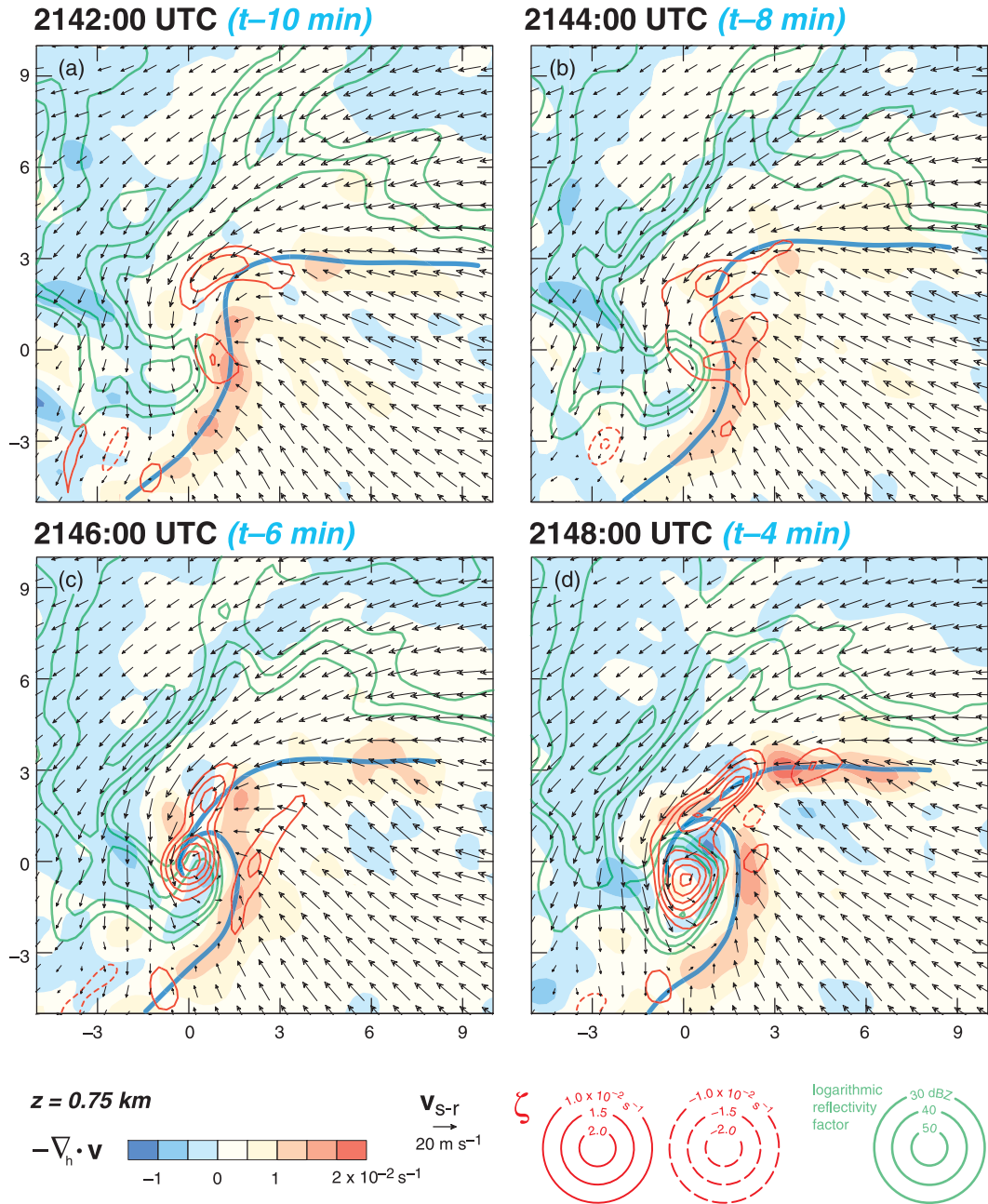


FIG. 11. Horizontal convergence ($-\nabla_h \cdot \mathbf{v}$; color), vertical vorticity (ζ ; red contours every 0.005 s^{-1} for $|\zeta| > 0.01 \text{ s}^{-1}$; negative contours are dashed), DOW7 logarithmic reflectivity factor (green contours every 10 dBZ for reflectivity ≥ 30 dBZ), and storm-relative wind vectors (\mathbf{v}_{S-R} ; plotted at every third grid point using black arrows) at $z = 0.75$ km obtained from the fine ($\kappa_0 = 0.48 \text{ km}^2$) dual-Doppler wind syntheses at (a) 2142:00, (b) 2144:00, (c) 2146:00, and (d) 2148:00 UTC. Gust fronts are indicated with heavy blue lines. Axis labels are in km.

(Figs. 7 and 8d,e). The intensification is unlikely attributable to a change in the geometry of the dual-Doppler sampling (dual-Doppler observations are available from the DOW6–DOW7 pair beginning at 2142 UTC). The vertical vorticity maxima and circulation derived from the first DOW6–DOW7 dual-Doppler wind synthesis at

2142 UTC, using the same amount of smoothing as in the KCYS–DOW7 dual-Doppler wind syntheses, compare well with the vertical vorticity maxima and circulation at 2139 UTC derived from the KCYS–DOW7 dual-Doppler wind synthesis (Fig. 7); that is, there is no obvious discontinuity in the time series at the time when

the radar pair is switched. Dual-Doppler wind syntheses derived from KCYS and DOW7 at 2144 and 2148 UTC (not shown) also compare well with the (smooth) dual-Doppler wind syntheses derived from DOW6 and DOW7 (Figs. 8d,e); the linear correlations between u , v , and w in the KCYS–DOW7 and DOW6–DOW7 wind syntheses at these two times were 0.98, 0.91, and 0.79, respectively. Moreover, the KCYS–DOW7 wind syntheses at 2144 and 2148 UTC also depict an intensification of low-level rotation during this time period.

The evolution of low-level ($z = 0.75$ km) vertical vorticity and horizontal convergence in the 2142–2148 UTC time period, derived from the comparatively high-resolution DOW6–DOW7 dual-Doppler observations ($\kappa_0 = 0.48 \text{ km}^2$), is shown in Fig. 11. The evolution of the vertical vorticity field is fairly complicated, with multiple maxima observed, typically along or in close proximity to the gust fronts. The most significant cyclonic vorticity maximum—the one ultimately associated with tornadogenesis at 2152 UTC—develops from a crescent-shaped region of vertical vorticity, east of the tip of the hook echo at 2144 UTC [centered near (0, 0) in Fig. 11b], within a region of horizontal convergence [this would be a region of positive vorticity stretching ($\xi\partial w/\partial z > 0$)]. The increase in vorticity and circulation is associated with an increase in northerly momentum on the western flank of the region of cyclonic rotation. A roughly west–east region of weak horizontal convergence [it extends from roughly (–5, –1) to (0, –3) in Fig. 11c] is located on the southern fringe of this northerly surge. This horizontal convergence band becomes more prominent at the later times analyzed by Kosiba et al. (2012, manuscript submitted to *Mon. Wea. Rev.*) and has been referred to as a *secondary gust front* (Wurman et al. 2007, 2010; Marquis et al. 2008, 2012).

Gust fronts have been subjectively analyzed by identifying wind shifts and corridors of horizontal convergence. Whereas the rear-flank gust front is well defined along most of its length, the forward-flank gust front is more diffuse, although it becomes increasingly well defined as tornadogenesis nears (cf. Figs. 11a,d). The rear-flank gust front “wraps up” during the period of rapid intensification, such that by 2148 UTC the primary cyclonic vertical vorticity maximum at low levels is surrounded by outflow and cut off from the environmental air to the southeast (Fig. 11d). Although the horizontal wind field is convergent at the center of the vortex, low-level divergence is associated with the downdraft that wraps around the vortex, nearly completely encircling it by 2148 UTC. A pocket of strong descent (e.g., $w \sim -20 \text{ m s}^{-1}$ at $z = 2$ km), probably an *occlusion downdraft* (Klemp and Rotunno 1983), is associated

with the patch of particularly strong horizontal divergence northeast of the vorticity maximum at (0.5, 0.5) in Fig. 11d.

The intensification of rotation described above occurred simultaneously with the development of a descending reflectivity core (DRC). There has been much recent interest in DRCs (Rasmussen et al. 2006; Kennedy et al. 2007a,b; Byko et al. 2009), given that they, upon reaching low levels, contribute to the formation or evolution of hook echoes and sometimes are observed to precede the rapid development or intensification of low-level rotation. Between 2130 and 2140 UTC, the evolution of the $w = 20 \text{ m s}^{-1}$ isosurface (Figs. 12a,b), in addition to horizontal cross sections of vertical velocity at midlevels (Figs. 13a,b), indicates the development of a new updraft pulse on the right flank of the main updraft. This pulse eventually grew into the main updraft by 2142 UTC (Figs. 12c and 13c). As this happened, reflectivity increased in a roughly 3-km-diameter column extending from an altitude of 4 to 7 km immediately behind (west of) the updraft (Fig. 12b), and this reflectivity core subsequently descended, reaching the surface in the 2142–2148 UTC period (Figs. 12c–f; a range of times is given because the exact time depends on which reflectivity isosurface is considered), precisely as low-level rotation was rapidly increasing (Fig. 7). Low-level rotation became particularly strong once the 55-dBZ (DOW7) reflectivity isosurface reached low levels (cf. Figs. 11c,d and 12e,f). The DRC descended down the interface that separated the RFD and backside of the updraft, within the hook echo and within a concave notch on the updraft’s rear flank (Fig. 14). The concavity of the updraft (Fig. 14), particularly at low levels, during the intensification of low-level rotation, is a well-known trait (e.g., Lemon and Doswell 1979).

As stated earlier, given the height of the data horizon during the period of KCYS–DOW7 dual-Doppler observation (2130–2142 UTC) and, as a result, the inability to observe low-level horizontal convergence below $z = 1.25$ km during that period, vertical velocity isosurfaces should be viewed only qualitatively.⁷ We are more confident that a distinct, new updraft maximum develops and grows into the main updraft than we are about its intensity. Our confidence that this updraft pulse was real is bolstered by its possible appearance in a photograph obtained from approximately 20 km east

⁷ Even at times when the data horizon is low, the errors in the vertical velocity field accumulate with altitude (e.g., Doviak et al. 1976); thus, *all* retrieved midlevel vertical velocities in this study should be interpreted only qualitatively (e.g., the maximum vertical velocities evident in Fig. 13 are not credible).

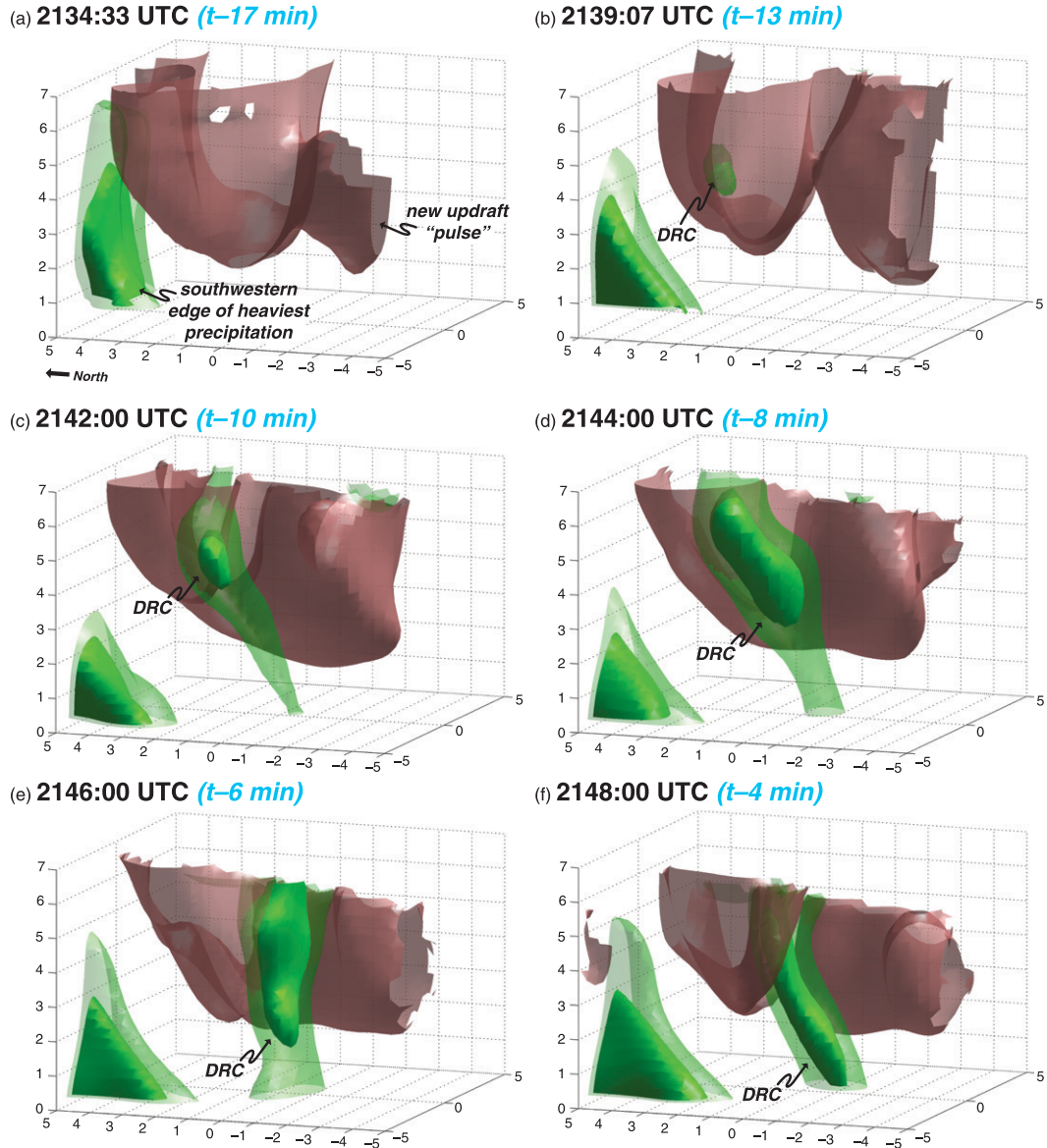


FIG. 12. View from the southwest of the 50- and 55-dBZ DOW7 reflectivity isosurfaces (green) and the 20 m s^{-1} vertical velocity isosurface (red) at (a) 2134:33, (b) 2139:07, (c) 2142:00, (d) 2144:00, (e) 2146:00, and (f) 2148:00 UTC. The vertical velocity field is from the smooth ($\kappa_0 = 2.64 \text{ km}^2$) dual-Doppler wind syntheses. Axis labels are in km.

of the storm at 2139 UTC (Fig. 9b; what we think might be the updraft pulse is labeled as “turret” in the photo). Unfortunately, no thermodynamic observations were obtained from the mobile mesonet within the DRC,⁸ nor were any disdrometers or dual-polarimetric radars deployed this early. StickNet probes (Weiss and

Schroeder 2008), which also obtained thermodynamic observations on 5 June 2009, were deployed farther to the east in anticipation of an extended intensive observing period. The descent rate of the DRC is sensitive to the choice of reflectivity isosurface [the 50 dBZ (55 dBZ) isosurface descends at 25 m s^{-1} (10 m s^{-1})], so unfortunately there are few clues from the reflectivity data about the microphysical characteristics of the DRC. However, given that the region in which the DRC was detected by radar was practically transparent visually (Figs. 9c,d), it is plausible that the DRC comprised sparse, large raindrops or hailstones.

⁸ Even if the mobile mesonet could have reached the storm earlier, it is unlikely that they would have been able to sample this region given the paucity of roads in the area; what few roads existed were generally unpaved and unfriendly to data collection in heavy precipitation.

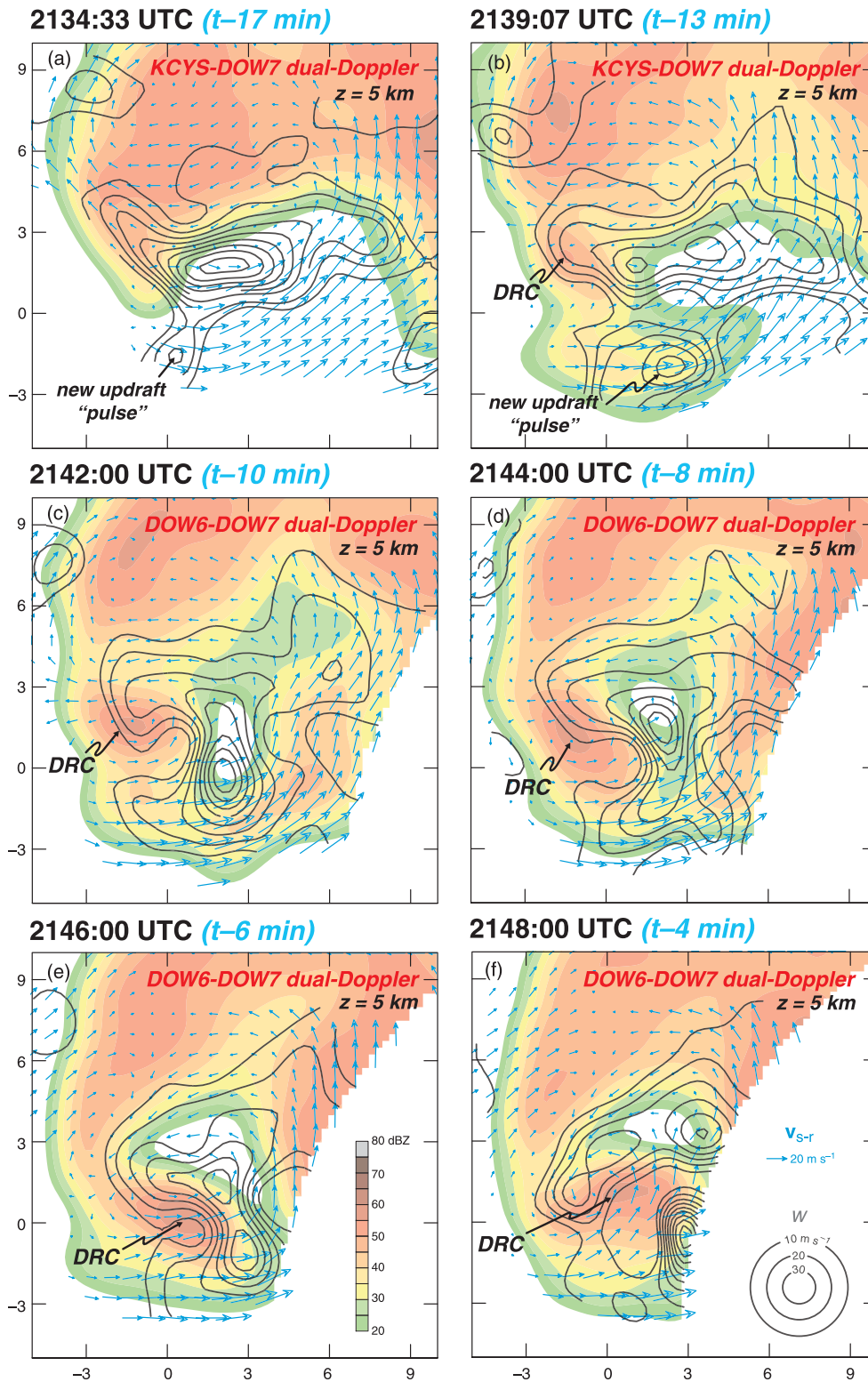


FIG. 13. Vertical velocity (w ; black contours) at $z = 5$ km obtained from the smooth ($\kappa_0 = 2.64 \text{ km}^2$) dual-Doppler wind syntheses at (a) 2134:33, (b) 2139:07, (c) 2142:00, (d) 2144:00, (e) 2146:00, and (f) 2148:00 UTC. Storm-relative wind vectors (v_{s-r}) are plotted at every third grid point at the same altitude using blue arrows. The wind syntheses in (a) and (b) are derived from the KCYS and DOW7 radars. The syntheses in (c)–(f) are derived from the DOW6 and DOW7 radars. Logarithmic reflectivity factor (color shading) is from DOW7 at $z = 5$ km. The DOW7 reflectivity is uncalibrated. Axis labels are in km.

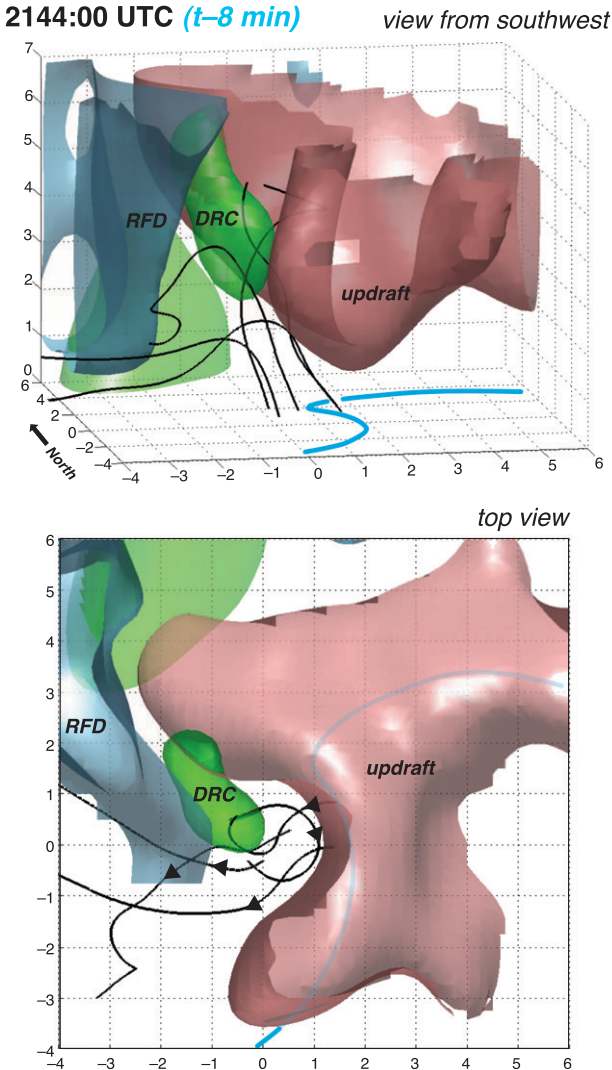


FIG. 14. Views from the southwest and from above of the 55-dBZ DOW7 reflectivity isosurface (green) and vertical velocity isosurfaces of -4 m s^{-1} (blue) and 20 m s^{-1} (red) at 2144 UTC (cf. Fig. 15a). The gust front is indicated with the heavy cyan line, and vortex lines that pass through the low-level mesocyclone are black (these are identical to those shown in Fig. 15a). The velocity field is derived from the smooth ($\kappa_0 = 2.64 \text{ km}^2$) dual-Doppler wind syntheses. Axis labels are in km. In the view from above, the direction of the vorticity vector is indicated by the arrowheads. Both the 50- and 55-dBZ reflectivity isosurfaces are shown in Fig. 12, but the 50-dBZ isosurface is suppressed above to improve the visibility of the other isosurfaces and vortex lines.

As the DRC descended, cyclonic and anticyclonic rotation initially intensified aloft, straddling the DRC (2144 UTC; Fig. 15a). Some of the vortex lines constructed in the vicinity of the low-level circulation form arches that join the counter-rotating vorticity extrema, but some of the vortex lines passing through the intensifying cyclonic vortex now also extend vertically

beyond the top of the data region (black lines in Fig. 15a). Note that the purple isosurfaces in Fig. 15 (cf. Fig. 10) are suppressed so that regions of very strong cyclonic vorticity (0.02 s^{-1} in the smooth dual-Doppler wind syntheses) are better revealed; the cyclonic vorticity is much stronger than the anticyclonic vorticity (this is also apparent in Fig. 11). The cyclonic (anticyclonic) “feet” of the arching vortex lines generally lie within convergence and updraft (divergence and downdraft), which probably accounts for the asymmetry of the vortex pair that straddles the DRC (Fig. 14). Davies-Jones et al. (2001) also attributed the favoring of the cyclonic vortex to its proximity to updraft. A similar preferential intensification of the cyclonic vortex has been seen in recent idealized numerical simulations designed to investigate, among other things, the sensitivity of vortex line “arching” to the location of the cold pool relative to the overlying updraft (Markowski et al. 2010). As was the case at the 2129 and 2139 UTC analysis times (Fig. 10), vortex lines drawn from the midlevel mesocyclone turn approximately horizontally near the base of the updraft and extend into the low-level environment to the south of the storm (dark blue lines in Fig. 15a).

By 2148 UTC, the 55-dBZ isosurface of the DRC extends to the surface (Fig. 12f), and a deep column of strong cyclonic rotation ($\zeta > 0.02 \text{ s}^{-1}$ in the smoothed dual-Doppler wind syntheses) is established from the surface to highest altitude of DOW6–DOW7 dual-Doppler coverage ($z \sim 7 \text{ km}$; Fig. 15b). Within this column, vertical vorticity gradually increases with height (in the fine dual-Doppler wind syntheses, the maximum vertical vorticity ranges from 0.033 s^{-1} at $z = 0.25 \text{ km}$ to 0.063 s^{-1} at $z = 6 \text{ km}$). All vortex lines passing within 1 km of the low-level vertical vorticity maximum extend vertically to the top of the data region. Arching vortex lines that connect the cyclonic vorticity with the anticyclonic vorticity trailing the hook echo still can be found by constructing vortex lines from a location several kilometers southeast of the cyclonic vorticity maximum (orange lines in Fig. 15b).

Although the maximum vertical vorticity at midlevels is now nearly directly over the maximum vertical vorticity at low levels—the result of upward advection and stretching in the column (not shown)—a distinct, separate cyclonic vorticity maximum associated with the tilting of environmental vortex lines still can be identified approximately 3 km farther east at midlevels (Fig. 15b). In contrast to the deep, strong cyclonic vortex present by this time, the anticyclonic vortex is not only weaker, but it does not extend to the surface, consistent with it being situated within divergence (which typically increases toward the surface) and downdraft. Moreover, the weaker anticyclonic vortex moves in a

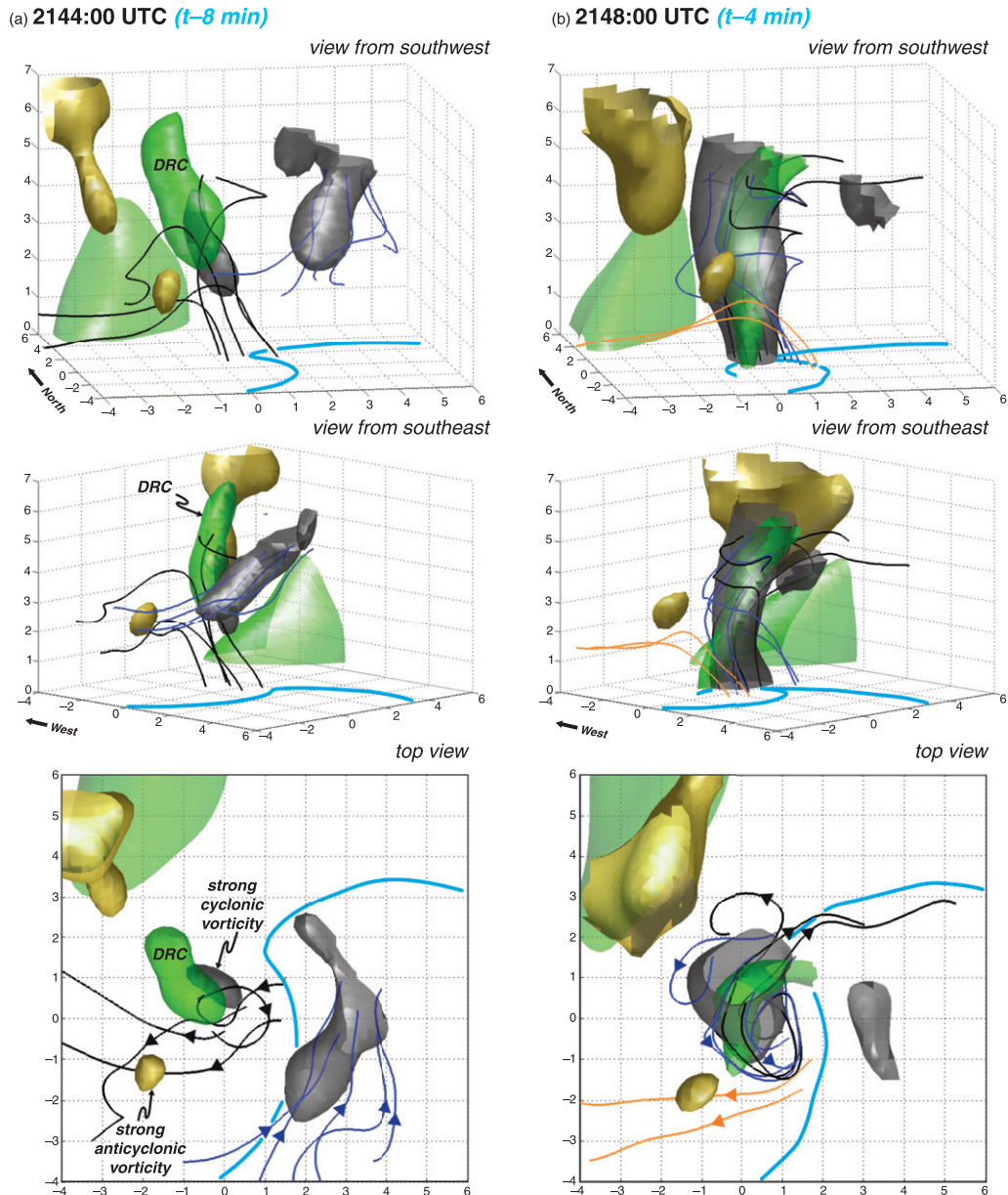


FIG. 15. Various 3D perspectives of the 55-dBZ DOW7 reflectivity isosurface (green) and vertical vorticity isosurfaces of 0.02 s^{-1} (gray) and -0.01 s^{-1} (yellow) at (a) 2144:00 and (b) 2148:00 UTC. The 0.01 s^{-1} vertical vorticity isosurfaces (the purple isosurfaces in Fig. 10) are suppressed to better reveal the intensification of rotation (i.e., the development of the 0.02 s^{-1} isosurface) in conjunction with the development of the DRC. Gust fronts are indicated with heavy cyan lines. Vortex lines that pass through the midlevel mesocyclone are blue. In (a), these lines pass through a lattice of five points centered on the vertical vorticity maximum at $z = 5 \text{ km}$, with one line passing through the maximum, and the other four lines passing through points that form a $1 \text{ km} \times 1 \text{ km}$ square centered on the maximum. In (b), the blue vortex lines that originate within the vorticity maximum at $z = 5 \text{ km}$, which is near the origin, extend almost straight downward to the surface, rather than turning horizontally and extending into the environment to the south (thus, the blue vortex lines in this figure do not originate in the environment, as was the case in Figs. 6 and 10). Vortex lines drawn from the midlevel vertical vorticity maximum centered at $(3, 0)$ (not shown), which is weaker than the midlevel maximum found near the origin at 2148 UTC, turn horizontally near the base of the updraft and extend into the environment to the south of the storm, as in (a). Vortex lines that pass through the low-level mesocyclone are black. These lines pass through a lattice of points at $z = 1.5 \text{ km}$ identical to the lattice at $z = 5 \text{ km}$, centered at the origin. Additional select vortex lines that pass through points in the vicinity of the low-level mesocyclone are orange. The vorticity field is derived from the smooth ($\kappa_0 = 2.64 \text{ km}^2$) dual-Doppler wind syntheses. In the view from above, the direction of the vorticity vector is indicated by the arrowheads. The reflectivity isosurfaces and vortex lines in (a) are identical to those shown in Fig. 14. Axis labels are in km.

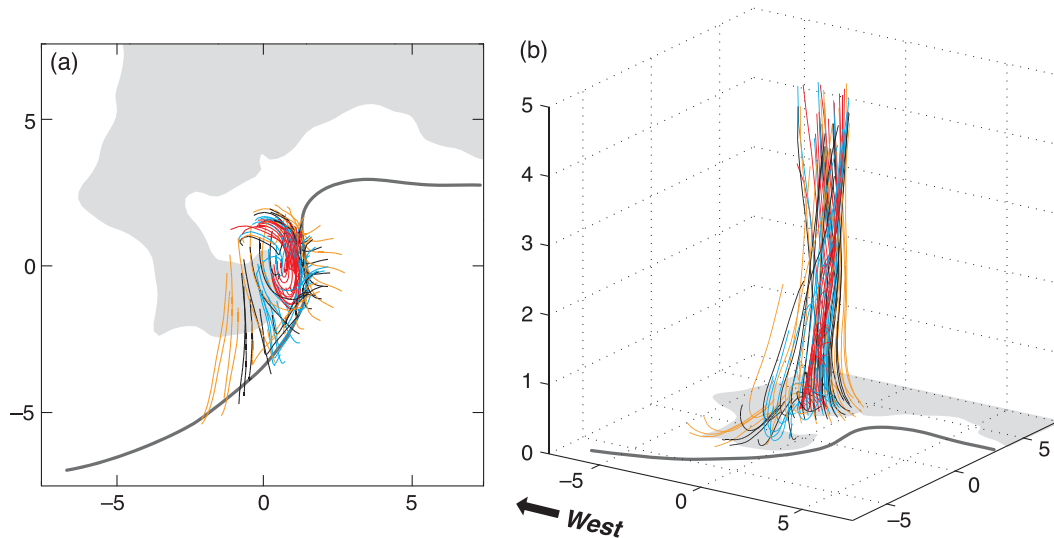


FIG. 16. View from (a) above and (b) to the southeast of trajectories integrated forward in time from 2142 to 2148 UTC in the region surrounding the vertical vorticity maximum at $z = 0.5$ km. Four rings comprising 20 parcels each are located at $z = 0.5$ km and surround the vertical vorticity maximum at 2142 UTC. The rings have the following radii: 0.5 km (red), 1.0 km (cyan), 1.5 km (black), and 2.0 km (orange). The 3D wind fields are based on the fine ($\kappa_0 = 0.48 \text{ km}^2$) dual-Doppler wind syntheses ($\kappa_0 = 0.48 \text{ km}^2$). Gray shading indicates DOW7 reflectivity factor at $z = 0.5$ km at 2142 UTC in excess of 30 dBZ. The gust front at 2142 UTC is indicated with the heavy black line. Axis labels are in km. The vertical scale is exaggerated.

counterclockwise direction around the stronger cyclonic vortex, reminiscent of the Fujiwhara (1931) effect (Figs. 15a,b).

Forward trajectories, originating near the surface in the vicinity of the intensifying low-level circulation, were computed from the fine ($\kappa_0 = 0.48 \text{ km}^2$) dual-Doppler-derived, three-dimensional velocity fields (Fig. 16) from 2142 to 2148 UTC.⁹ At 2142 UTC, four rings comprising 20 parcels each are located at $z = 0.25$ km and surround the vertical vorticity maximum. The rings have radii of 0.5, 1.0, 1.5, and 2.0 km. The vast majority of the trajectories rapidly rise to the top of the data region by 2148 UTC. Exceptions are the trajectories in the western portion of the two outermost rings, which descend (note the orange trajectories near $x = -2$ km in Fig. 16).

The abrupt ascent of the trajectories during the intensification of the low-level circulation is perhaps not surprising, and is similar to what has been seen in other tornadic storms [cf. Fig. 9 of Markowski et al. (2011)]. However, the characteristics of the trajectories stand in

contrast to the characteristics of trajectories observed in several nontornadic supercells, in which the trajectories passing through the near-surface vertical vorticity maxima had comparatively shallow upward vertical excursions, suggesting that the parcels passing through the near-surface circulations did not enter the overlying midlevel updraft and mesocyclone [cf. Fig. 7 of Markowski et al. (2011)].

b. Surface thermodynamic observations and downdraft characteristics

Subjective analyses of virtual potential temperature θ_v and equivalent potential temperature¹⁰ θ_e derived from the mobile mesonet observations were produced from 10-min windows of observations centered on 2140 and 2148 UTC (Fig. 17). Most of the observations upon which the analyses were based were obtained within 2.5 min of the analysis times because, in the case of spatially proximate observations, the closest to the analysis time was used. Thermodynamic retrievals using the three-dimensional wind fields were attempted (these

⁹ The trajectories were integrated using a fourth-order Runge-Kutta algorithm (as was done for the vortex lines). A time step of 15 s was used, and the 3D wind fields were assumed to vary linearly in time between dual-Doppler analyses. The spatial interpolation was trilinear.

¹⁰ Bolton's (1980) formula for pseudoequivalent potential temperature was used. When referring to θ_e throughout the article, we technically are referring to pseudoequivalent potential temperature, which is conserved for dry adiabatic and pseudoadiabatic processes.

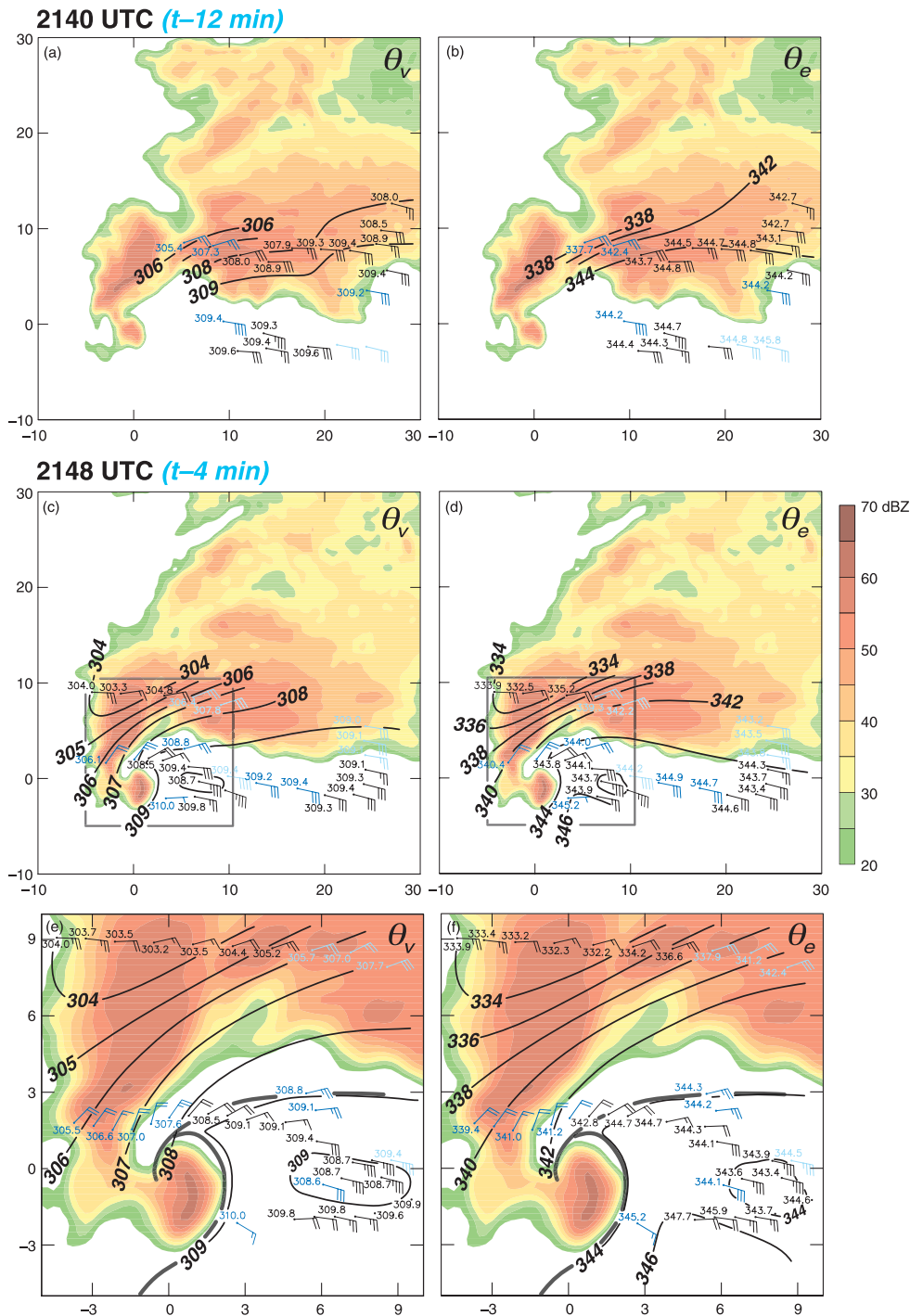


FIG. 17. Subjective analyses of virtual potential temperature (θ_v ; K) and equivalent potential temperature (θ_e ; K) derived from mobile mesonet observations at (a), (b) 2140 UTC and (c)–(f) 2148 UTC [the region enclosed by the gray box in (c) and (d) is enlarged in (e) and (f)]. The time-to-space conversion used to create the analyses assumed a steady state for a 10-min period centered on the analysis times. Station models depict storm-relative winds (half barb = 2.5 m s^{-1} ; full barb = 5 m s^{-1}) and either θ_v or θ_e values, depending on which field is analyzed. Observations within 2.5 min of the analysis time are black; observations obtained more than 2.5 min after (before) the analysis time are dark (light) blue. The objectively analyzed logarithmic reflectivity factor (dBZ) from the DOW7 radar at $z = 0.5 \text{ km}$ is displayed in the background in each panel. The gust fronts derived from the dual-Doppler wind synthesis are indicated with gray lines in (e) and (f) (cf. Fig. 11d). Axis labels are in km. Values of θ_e were computed using Bolton's (1980) formula for pseudoequivalent potential temperature.

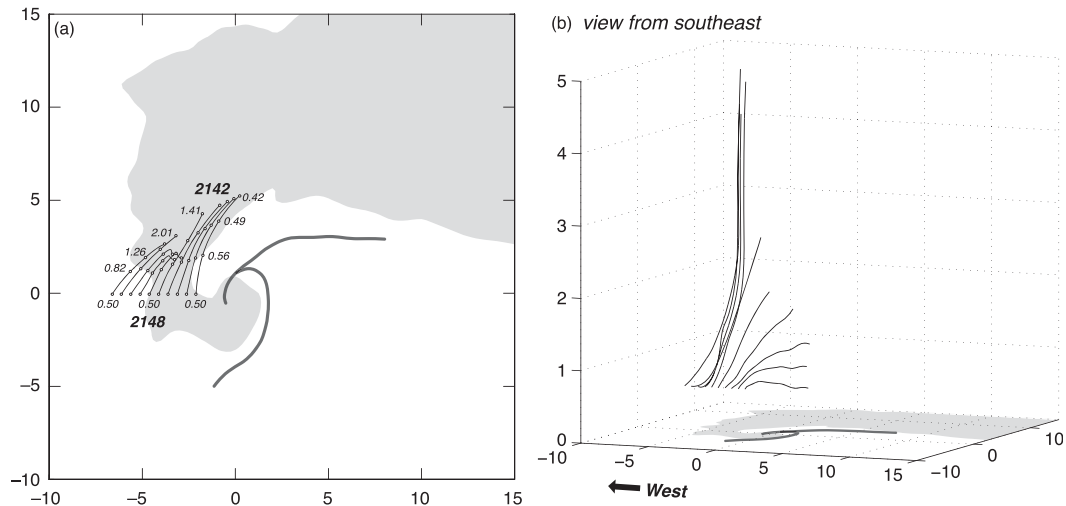


FIG. 18. (a) Downdraft trajectories integrated backward from 2148 to 2142 UTC. At 2148 UTC, the parcels are evenly spaced at $z = 0.5$ km and comprise a west–east line from 2–7 km west of the vertical vorticity maximum at that level. The 3D wind fields are based on the fine ($\kappa_0 = 0.48 \text{ km}^2$) dual-Doppler wind syntheses. Markers appear along the trajectories every 2 min, and select markers are accompanied by labels indicating the height of the trajectory (km). Gray shading indicates DOW7 reflectivity factor at $z = 0.5$ km at 2148 UTC in excess of 30 dBZ. Gust fronts at 2148 UTC are indicated with the heavy black lines. (b) Three-dimensional perspectives of the trajectories viewed from the southeast. The vertical scale is exaggerated. Axis labels in (a) and (b) are in km.

would have the enormous benefit of greater spatial coverage, as well as information about thermodynamic fields aloft), but were found to be insufficiently reliable. Although a “momentum checking” parameter (E_r ; Gal-Chen 1978) in the 0.2–0.3 range always could be obtained if the input wind velocity gradients were sufficiently smoothed—smoothing that augmented the smoothing applied in the interpolation of the radial velocity data to the grid on which the wind syntheses were performed—the retrieved buoyancy fields had poor temporal continuity (correlations between one analysis and another only 2 min later were occasionally nearly zero) and compared poorly with in situ mobile mesonet observations, where available (correlations with in situ observations were occasionally *negative*, and even the best retrievals had rms errors of 2–3 K). The reasons for the poor retrievals are beyond the scope of this article, but likely include relatively coarse temporal resolution of the evolving wind velocity field and discretization errors owing to the numerous spatial derivatives required in the retrievals (Majcen et al. 2008).

The 2140 UTC analyses are limited to the forward flank of the storm (Figs. 17a,b), given that the mobile mesonet was only arriving at the storm during this analysis period. The mobile mesonet sampled a roughly southward-pointing θ_v gradient of approximately $3 \text{ K } (5 \text{ km})^{-1}$ along the southern flank of the forward-flank radar echo, with θ_v varying from $\sim 309 \text{ K}$ along the southern edge of the echo to $\sim 306 \text{ K}$ approximately 5 km farther north

(Fig. 17a). No attempt was made to quantify the contribution to negative buoyancy from hydrometeors using DOW reflectivities (KCY5 was not considered because of its distance and data horizon), given the uncertainties intrinsic to the parameterization of hydrometeor mass from reflectivity, and the aforementioned DOW reflectivity issues (i.e., uncalibrated reflectivity factors and the possibility of Mie scattering in high-reflectivity regions). However, it is probably safe to assume that hydrometeor mass in the region of highest reflectivity easily could have contributed the equivalent of a -2-K temperature perturbation to the negative buoyancy,¹¹ which would yield a horizontal density potential temperature (θ_ρ ; Emanuel 1994, p. 161) gradient of roughly 1 K km^{-1} .¹² Mobile mesonet storm-relative winds (2 m AGL) were approximately easterly within the region of largest analyzed θ_v (or θ_ρ) gradient, implying the baroclinic generation of streamwise horizontal vorticity there. The horizontal θ_e gradient in the forward flank had a similar orientation, but was larger in magnitude. Our analysis implies a maximum gradient of approximately 2 K km^{-1} [e.g., near (8, 8) in Fig. 17b].

¹¹ This would require a hydrometeor mixing ratio of roughly 7 g kg^{-1} .

¹² To put this gradient into perspective, a parcel of air residing in a 1 K km^{-1} horizontal θ_ρ gradient would acquire a horizontal vorticity of 0.01 s^{-1} in 5 min.

The 2148 UTC analyses include transects of mobile mesonet probes across the hook echo and the portion of the radar echo north through northwest of the updraft (Figs. 17c–f). The portion of the RFD that was sampled (the west–east transect at $y = 1.5$ km in Fig. 17e) is not particularly cold; θ_v gradually drops from ~ 309 K, from a point just northeast of the tip of the hook echo [near (2, 2) in Fig. 17e], to 305.5 K at the rear of the hook echo, 6 km to the west, with θ_v of 306–307 K within the hook echo at the latitude of the observations. Although the outflow encircling the low-level circulation and tip of the hook echo was unsampled at this time because of the lack of roads, the forward trajectories computed from this region (Fig. 16) might be an indication that this air had relatively small negative buoyancy, similar to the relatively small negative buoyancy implied by the observations farther upstream (north) and within the hook echo. The rapid ascent of nearly all of the trajectories originating within 2 km of the low-level vorticity maximum is only possible if the upward-directed, vertical perturbation pressure gradient force (VPPGF) exceeds the negative buoyancy, the likelihood of which increases as the negative buoyancy of the parcels decreases. Moreover, the θ_e deficits of the upstream hook-echo/RFD air were relatively small; the θ_e within the aforementioned transect of the hook echo and RFD was generally >340 K (Fig. 17f), which is associated with surface-based CAPE (SBCAPE) in excess of 1500 J kg⁻¹ per the 2155 UTC proximity sounding (Fig. 2a). Observations nearer to the circulation center obtained later, after roughly 2200 UTC, reveal that the air in the near-mesocyclone region was not exceptionally cold (θ_v deficits remained <3 K within 2 km of the circulation, where observations were available) during the time the tornado was intensifying (Kosiba et al. 2012, manuscript submitted to *Mon. Wea. Rev.*), although we cannot easily assess the contribution of hydrometeors to the buoyancy field at the later times either.

Additional insight about the θ_e field within the hook echo and RFD region is gained from backward trajectories initiated at 2148 UTC (Fig. 18). The trajectories originate at $z = 0.5$ km within a west–east line from 2 to 7 km west of the vertical vorticity maximum at that level, and were integrated backward to 2142 UTC. The trajectories were computed using the fine ($\kappa_0 = 0.48$ km²) dual-Doppler wind syntheses. The downward (going forward in time) excursions of the trajectories increase from east to west, and the θ_e values observed at the surface within the rear-flank outflow are negatively correlated with the magnitudes of the downward vertical excursions; that is, the regions of lowest θ_e at the surface correspond to the regions where air descends from the highest altitudes (cf. Figs. 17f and 18). The trajectories

that are only 2–4 km west of the vertical vorticity maximum at 2148 UTC have relatively shallow trajectories that descend gently from the forward flank. Several of these never get above $z = 1$ km and, based on nearby mobile mesonet observations, are associated with θ_e values only a few degrees (K) cooler than the environmental inflow values. The trajectories closest to the vorticity maximum exhibit characteristics resembling the high- θ_e “up–down” downdraft identified by Knupp and Cotton (1985). In contrast, trajectories that are 4–7 km west of the vertical vorticity maximum at 2148 UTC descend from considerably higher altitudes ($z = 2$ –4 km; Fig. 18). A comparison of the θ_e profile on the proximity sounding (Fig. 2c) to the θ_e observations obtained at the surface near the region where trajectories descend from the highest altitudes (Fig. 17f) suggests that the downdraft parcels are a mixture of low- θ_e environmental air and high- θ_e updraft air. This claim is based on the fact that the environmental θ_e is ~ 325 K from 2 to 4 km AGL, yet nowhere at the surface were θ_e values observed to be this low.

The coldest air sampled within the storm in the pre-tornadic phase was located ~ 9 km north of the circulation center at 2148 UTC, where θ_v approached 303 K, which represents a deficit (relative to the inflow immediately southeast of the gust front) of ~ 6.5 K (Figs. 17c,e). The mean horizontal θ_v gradient from this location to a point to the southeast along the analyzed forward-flank gust front [i.e., in the direction of the θ_v gradient, from (0, 9) to (4.5, 3)] is roughly 6 K (7.5 km)⁻¹. Including the effects of hydrometeor loading, the mean horizontal gradient of θ_p is virtually certain to exceed 1 K km⁻¹ over the same distance, although the gradient is likely much larger to the northwest [e.g., in proximity to (1, 7)] than to the southeast [e.g., in proximity to (4.5, 3)]. As was the case for the 2140 UTC analysis, the θ_e gradient analyzed at 2148 UTC points in approximately the same direction as the θ_v gradient, and is roughly twice the magnitude (Figs. 17d,f).

5. Discussion

a. The origin of the DRC

What caused the DRC? The formation of the DRC shares similarities with both the type-I and type-II DRCs noted by Byko et al. (2009) in numerical simulations. Type-I DRCs formed as a result of updraft intensification, followed by the accumulation of increased rainwater in a “stagnation zone” (i.e., a region in which the storm-relative winds nearly vanished) on the upshear flank of the midlevel updraft and eventual descent of this precipitation once fall speeds became sufficiently

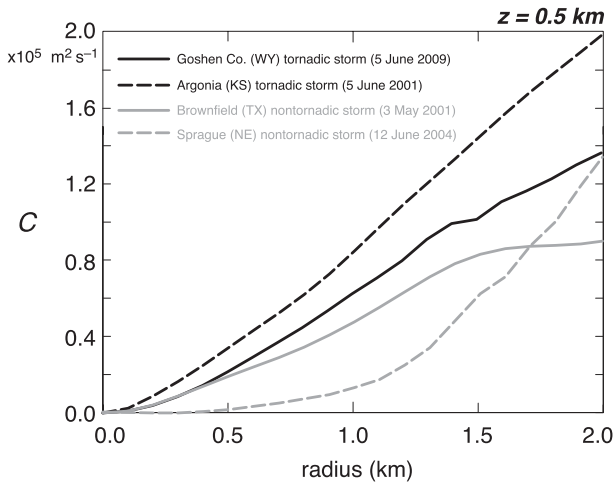


FIG. 19. Radial profiles of circulation at $z = 0.5$ km for the Goshen County mesocyclone at 2148 UTC. The profiles of circulation also are shown for three other mesocyclones observed by the DOW radars 5 min prior to tornadogenesis or, in the case of the nontornadic mesocyclones, 5 min prior to the time of maximum low-level rotation [see Markowski et al. (2011) for further details; dual-Doppler data were obtained for all three cases].

large. Type-II DRCs were attributed to precipitation that formed within a new updraft that eventually merged with the main updraft, a process that occurred in conjunction with updraft–mesocyclone “cycling.”

In the Goshen County storm, some aspects of the “new updraft” paradigm (i.e., the type-II DRC) are present (the similarity between our Figs. 12 and 13 and Byko et al.’s Figs. 17 and 18 is stunning). However, evidence of a more complicated evolution, such as the accumulation of precipitation on the upshear flank of the midlevel updraft, also is present in the Goshen County storm, similar to the type-I DRCs (cf. our Fig. 13 and Byko et al.’s Fig. 14). Figure 13 suggests a complex evolution in the reflectivity field due to a combination of horizontal advection of hydrometeors and presumably changes in hydrometeor concentration resulting from condensation and fallout. It is also tempting to wonder whether it was merely a coincidence that the upward-growing $\zeta = 0.01 \text{ s}^{-1}$ isosurface, originating in the outflow and associated with arching vortex lines, merged with the $\zeta = 0.01 \text{ s}^{-1}$ isosurface associated with the midlevel mesocyclone and environmental vortex lines just before the DRC developed (cf. Figs. 10 and 12b). Could changes in the midlevel wind field associated with the “arching process” somehow have instigated the DRC?

If the new updraft pulse evident in Figs. 9b, 12a,b, and 13a,b did indeed play a key role in the formation of the DRC, this naturally leads to additional questions. What instigated the new updraft pulse? Environmental heterogeneity encountered by the storm? Internal dynamics?

Supercells, though often envisioned as quasi-steady, are well known to exhibit periodic new updraft development, although the spacing between subsequent pulses in space and time is smaller for supercells than multicell storms (Brandes 1993). Are the precipitation processes associated with these new pulses potentially tornadogenesis instigators? Further speculation as to the origin of the DRC is limited by the lack of microphysical observations and accurate air parcel trajectories (let alone hydrometeor trajectories) at this altitude, and is therefore beyond the scope of this article.

b. Comparison to nontornadic supercells

We emphasize that the evolution described in this article, and the dynamics that will be examined in Part II, are not necessarily unique to tornadic supercells. We only have documented the development of low-level circulation and its increase in the minutes leading up to tornadogenesis. The vertical vorticity increased by another order of magnitude in the 2148–2158 UTC period (the “tornadogenesis period”; Kosiba et al. 2012, manuscript submitted to *Mon. Wea. Rev.*).

The circulation associated with the Goshen County low-level mesocyclone at the end of our analysis period (i.e., 2148 UTC, which is 4 min before the vortex first reached tornado strength in DOW observations) was not remarkably stronger than the circulation associated with weakly tornadic and nontornadic low-level mesocyclones observed at a similar stage in their evolution with datasets having comparable spatial resolution (Fig. 19). For example, at a radius of 2 km from the low-level circulation center, the Goshen County storm had the same circulation as that observed in the Sprague, Nebraska, nontornadic supercell (12 June 2004) documented by Markowski et al. (2011). The pretornadic low-level mesocyclone of the Argonia, Kansas, tornadic supercell (5 June 2001; Dowell et al. 2002) had larger circulation than the low-level mesocyclone of the Goshen County storm at all radii within 2 km of the low-level circulation center, despite the former storm only producing a short-lived, weak (F0) tornado.

The development of low-level circulation is obviously a necessary but insufficient condition for tornadogenesis. The buoyancy of the outflow that acquires large circulation, in addition to the magnitude of the upward-directed VPPGF, are as important as the magnitude of the circulation. Material circuits surrounding the circulation center only can contract if they encircle air that can be accelerated upward (i.e., the negative buoyancy of the air must be overcome by the upward-directed VPPGF). Although there is uncertainty in the contribution to the negative buoyancy from hydrometeors, the θ_v deficits upstream (i.e., north and north-northeast) of

the Goshen County storm's low-level mesocyclone were relatively small as tornadogenesis neared (~ 3 K at most; Fig. 17e), as has been seen in other tornadic supercells (e.g., Markowski et al. 2002; Grzych et al. 2007). Perhaps not surprisingly, the vast majority of the trajectories in this region all rose rapidly in the 2142–2148 UTC period, as discussed in section 4a (Fig. 16). Moreover, the aforementioned outflow parcels, as pointed out in section 4b, also possessed significant CAPE. Both the buoyancy (related to the instantaneous vertical acceleration) and the CAPE (related to the *potential* buoyancy) of the outflow parcels would seem to be relevant to tornadogenesis. Parcels possessing significant CAPE would have the potential to ascend through the entire depth of the storm updraft; stagnation at a low altitude, just above an intensifying surface vortex, would not seem to favor the intensification of a vortex to tornado strength. Moreover, in theoretical studies (e.g., Fiedler and Rotunno 1986), the maximum intensity of a tornado is related to the CAPE. Although it is not entirely straightforward to apply these conclusions to an actual storm, it would seem that the CAPE of the *outflow* must have at least some relevance, given that it is the angular momentum of parcels within the outflow that is converged in tornadogenesis, at least in cases in which the environment contains no significant preexisting vertical vorticity.

6. Summary and conclusions

This article has documented the pretornadic phase of the 5 June 2009 tornadic supercell intercepted by VORTEX2 in Goshen County, Wyoming, from the time the storm first exhibited supercell characteristics (~ 2100 UTC) until 2148 UTC, which was 4 min before mobile radars observed a tornado-strength vortex. The evolution of the storm during the period of dual-Doppler observations (2130–2148 UTC) is summarized in Fig. 20.

At the time that dual-Doppler data collection began, the regions of significant ($\geq 10^{-2} \text{ s}^{-1}$) midlevel and low-level cyclonic vorticity were separated, per isosurface analyses, with the low-level mesocyclone located along the gust front and the midlevel mesocyclone leading the low-level mesocyclone by several kilometers (Figs. 10a and 20a). Vortex lines associated with the midlevel mesocyclone originated in the environment to the south. In contrast, vortex lines associated with the low-level mesocyclone formed arches that joined the cyclonic vorticity region with a mesoanticyclone in the outflow trailing the hook echo. The configuration of these vortex lines suggests that they were generated or strongly modified by baroclinicity.

Although the maximum vertical vorticity at low levels and midlevels was fairly constant from 2130 to 2142 UTC (and single-Doppler observations of azimuthal wind shear suggest that the relatively steady state extended to earlier times as well; Fig. 7), the region of significant cyclonic vertical vorticity at low levels gradually grew upward and into the region of significant midlevel vertical vorticity, resulting in a single column of vertical vorticity that spanned the depth of the radar observations by 2140 UTC (Figs. 10b and 20b). A DRC then developed at midlevels to the rear of the updraft, and its descent to the surface was accompanied by the rapid intensification of cyclonic vorticity at low and midlevels (Figs. 20c,d). Anticyclonic vorticity also intensified, though to a far lesser degree than the amplification of cyclonic vorticity.

By 2148 UTC, the gust fronts had acquired a familiar occluded structure, with the rear-flank gust front having wrapped around the circulation center. Strong rotation ($\zeta > 0.02 \text{ s}^{-1}$) extended from the lowest levels scanned by the radars to midlevels, although two distinct vorticity maxima could still be identified at midlevels. One was associated with environmental vortex lines that had been tilted to form the original midlevel mesocyclone, and the other was associated with the upward development of the vortex line arches that originated in the outflow at low levels. The tornado that developed in the ensuing minutes was associated with this deep column of strong rotation.

We have high confidence in the following conclusions:

- 1) The θ_v observed at the surface, within the outflow, a short distance (~ 3 km) upstream of the circulation center, was no more than 3 K colder than the warmest θ_v readings in the inflow of the storm. Larger θ_v deficits (up to 6 K) were observed to the rear of the hook echo and within the heavy precipitation to the north of the updraft.
- 2) The θ_e field observed at the surface had a structure similar to the θ_v field (i.e., θ_e decreased within the outflow to the west and northwest). The regions of lowest θ_e at the surface corresponded to the regions where air had descended from the highest altitudes.
- 3) Forward trajectories originating in the intensifying low-level mesocyclone rose rapidly in the 2142–2148 UTC period (in contrast to the trajectories originating in some nontornadic low-level mesocyclones that have been documented recently). The upward accelerations imply that the upward-directed VPPGF exceeded the negative buoyancy.
- 4) The rapid increase in low-level vertical vorticity and circulation (about a fixed ring encircling the vertical vorticity maximum) in the 2142–2148 UTC period was preceded by a DRC.

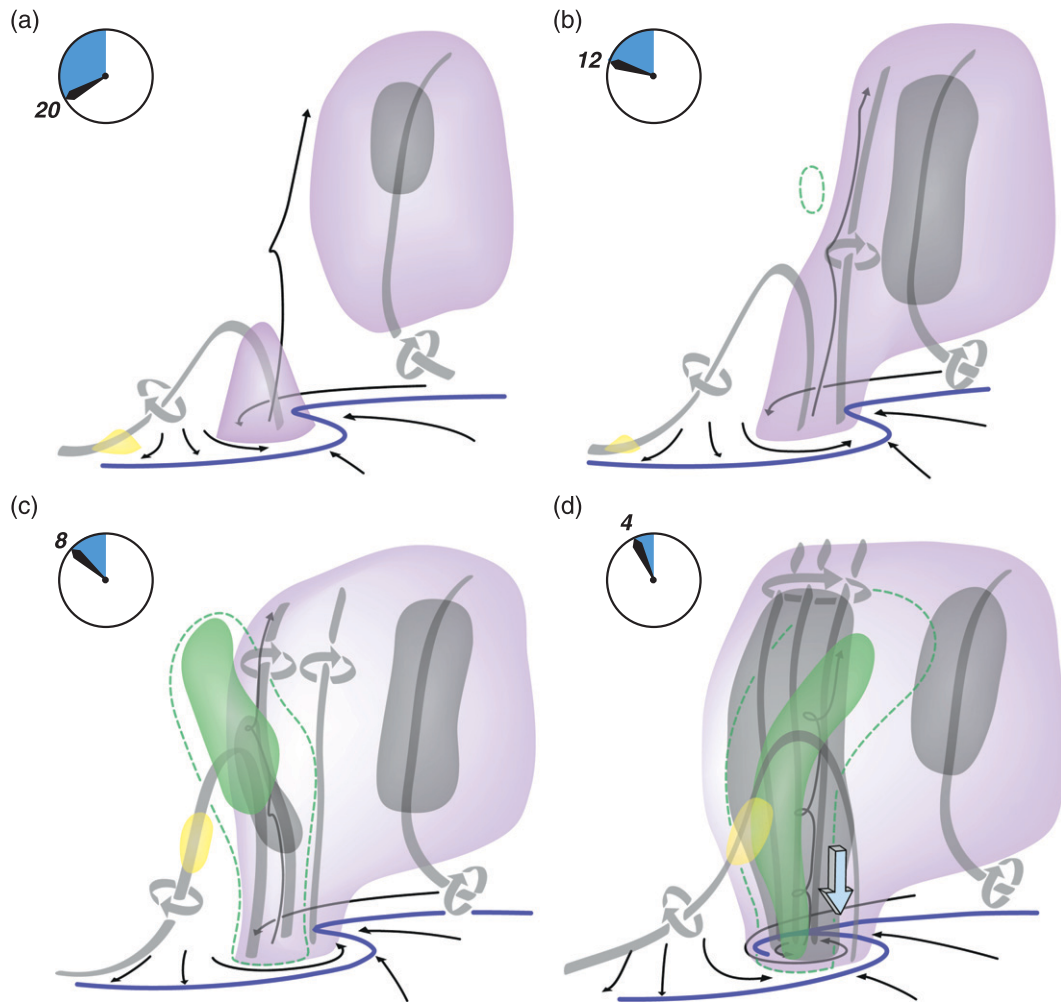


FIG. 20. Schematic summarizing the evolution of the Goshen County storm during its pretornadic phase: (a) 2130–2135 (~20 min prior to tornadogenesis, as indicated by the hand on the clock), (b) 2135–2140 (~12 min prior to tornadogenesis), (c) 2142–2144 (~8 min prior to tornadogenesis), and (d) 2146–2148 UTC (~4 min prior to tornadogenesis). The yellow and purple isosurfaces indicate regions of significant anticyclonic and cyclonic vorticity, and the dark gray isosurfaces enclose regions of even larger cyclonic vorticity. The DRC is indicated by the green dashed line and green isosurface (they enclose reflectivities in excess of 50 and 55 dBZ, respectively). Surface gust fronts are analyzed using blue lines. Streamlines are drawn using black arrows. Vortex lines are gray (the sense of rotation is indicated by the gray arrows). In (d), the broad downward-pointing arrow indicates an occlusion downdraft.

5) The DRC was practically transparent visually, as viewed from the east-southeast.

The conclusions inspire several additional questions, none of which we can answer at this point, unfortunately. What caused the DRC? What are its microphysical characteristics? Would the intensification of low-level rotation have happened eventually without the DRC?

Part II explores the dynamical role of the DRC, as well as the general question of the relative contributions of environmental vorticity and storm-generated vorticity to the rotation of the low-level mesocyclone.

Acknowledgments. We are grateful for the support of VORTEX2 by the National Science Foundation (NSF) and National Oceanic and Atmospheric Administration. The authors were supported by awards AGS-0801035, AGS-0801041, and AGS-1036237 made to PSU, CSWR, and Rasmussen Systems, respectively. We also thank the countless number of VORTEX2 PIs, students, and other participants, without which the project would not have been possible. Radar data were edited using the SOLOII software provided by the Earth Observing Laboratory at the National Center for Atmospheric Research (NCAR). Jim LaDue provided the

photograph in Fig. 9b. The video frames in Figs. 9c,d are courtesy of Nolan Atkins, Roger Wakimoto, and the Lyndon State University–NCAR photogrammetry group. The DOW radars are NSF Lower Atmospheric Observing Facilities supported by AGS-0734001. Lastly, we appreciate the selfless donation of time and constructive comments provided by the reviewers (Chris Weiss, Morris Weisman, and one anonymous reviewer) and editor (George Bryan).

REFERENCES

- Barnes, S. L., 1964: A technique for maximizing details in numerical weather map analysis. *J. Appl. Meteor.*, **3**, 396–409.
- Bolton, D., 1980: The computation of equivalent potential temperature. *Mon. Wea. Rev.*, **108**, 1046–1053.
- Brandes, E. A., 1977: Flow in severe thunderstorms observed by dual-Doppler radar. *Mon. Wea. Rev.*, **105**, 113–120.
- , 1993: Tornadic thunderstorm characteristics determined with Doppler radar. *The Tornado: Its Structure, Dynamics, Prediction, and Hazards, Geophys. Monogr.*, Vol. 79, Amer. Geophys. Union, 143–159.
- Byko, Z., P. Markowski, Y. Richardson, J. Wurman, and E. Adlerman, 2009: Descending reflectivity cores in supercell thunderstorms observed by mobile radars and in a high-resolution numerical simulation. *Wea. Forecasting*, **24**, 155–186.
- Davies-Jones, R. P., 1984: Streamwise vorticity: The origin of updraft rotation in supercell storms. *J. Atmos. Sci.*, **41**, 2991–3006.
- , R. J. Trapp, and H. B. Bluestein, 2001: Tornadoes and tornadic storms. *Severe Convective Storms, Meteor. Monogr.*, No. 50, Amer. Meteor. Soc., 167–221.
- Doviak, R. J., P. S. Ray, R. G. Strauch, and L. J. Miller, 1976: Error estimation in wind fields derived from dual-Doppler radar measurement. *J. Appl. Meteor.*, **15**, 868–878.
- Dowell, D. C., and A. Shapiro, 2003: Stability of an iterative dual-Doppler wind synthesis in Cartesian coordinates. *J. Atmos. Oceanic Technol.*, **20**, 1552–1559.
- , Y. Richardson, and J. Wurman, 2002: Observations of the formation of low-level rotation: The 5 June 2001 Sumner County, Kansas tornado. Preprints, *21st Conf. on Severe Local Storms*, San Antonio, TX, Amer. Meteor. Soc., 12.3. [Available online at <http://ams.confex.com/ams/pdfpapers/47335.pdf>.]
- Emanuel, K. A., 1994: *Atmospheric Convection*. Oxford University Press, 580 pp.
- Fiedler, B. H., and R. Rotunno, 1986: A theory for the maximum wind speeds in tornado-like vortices. *J. Atmos. Sci.*, **43**, 2328–2340.
- Fujiwhara, S., 1931: Short note on the behavior of two vortices. *Proc. Phys. Math. Soc. Japan*, **13**, 106–110.
- Gal-Chen, T., 1978: A method for the initialization of the anelastic equations: Implications for matching models with observations. *Mon. Wea. Rev.*, **106**, 587–606.
- Grzych, M. L., B. D. Lee, and C. A. Finley, 2007: Thermodynamic analysis of supercell rear-flank downdrafts from Project ANSWERS. *Mon. Wea. Rev.*, **135**, 240–246.
- Kennedy, A. D., E. N. Rasmussen, and J. M. Straka, 2007a: A visual observation of the 6 June 2005 descending reflectivity core. *Electron. J. Severe Storms Meteor.*, **2** (6).
- , J. M. Straka, and E. N. Rasmussen, 2007b: A statistical study of the association of DRCs with supercells and tornadoes. *Wea. Forecasting*, **22**, 1192–1199.
- Klemp, J. B., and R. Rotunno, 1983: A study of the tornadic region within a supercell thunderstorm. *J. Atmos. Sci.*, **40**, 359–377.
- Knupp, K. R., and W. R. Cotton, 1985: Convective cloud downdraft structure: An interpretive survey. *Rev. Space Phys. Geophys.*, **23**, 183–215.
- Koch, S. E., M. DesJardins, and P. J. Kocin, 1983: An interactive Barnes objective map analysis scheme for use with satellite and conventional data. *J. Climate Appl. Meteor.*, **22**, 1487–1503.
- Leise, J. A., 1982: A multidimensional scale-telescoped filter and data extension package. NOAA Tech. Memo. ERL WPL-82, 19 pp. [Available from NOAA Office of Oceanic and Atmospheric Research, Silver Spring Metro Center, Bldg 3, Room 11627, Silver Spring, MD 20910.]
- Lemon, L. R., and C. A. Doswell III, 1979: Severe thunderstorm evolution and mesocyclone structure as related to tornado genesis. *Mon. Wea. Rev.*, **107**, 1184–1197.
- Majcen, M., P. Markowski, Y. Richardson, D. Dowell, and J. Wurman, 2008: Multipass objective analyses of Doppler radar data. *J. Atmos. Oceanic Technol.*, **25**, 1845–1858.
- Markowski, P. M., and Y. P. Richardson, 2008: The structure and evolution of vortex lines in supercell thunderstorms. Preprints, *24th Conf. on Severe Local Storms*, Savannah, GA, Amer. Meteor. Soc., 4.1. [Available online at http://ams.confex.com/ams/24SLS/techprogram/paper_141560.htm.]
- , J. M. Straka, and E. N. Rasmussen, 2002: Direct surface thermodynamic observations within the rear-flank downdrafts of nontornadic and tornadic supercells. *Mon. Wea. Rev.*, **130**, 1692–1721.
- , E. N. Rasmussen, J. M. Straka, R. P. Davies-Jones, Y. Richardson, and J. Trapp, 2008: Vortex lines within low-level mesocyclones obtained from pseudo-dual-Doppler radar observations. *Mon. Wea. Rev.*, **136**, 3513–3535.
- , M. Majcen, and Y. Richardson, 2010: Near-surface vortex genesis in idealized three-dimensional numerical simulations involving a heat source and a heat sink in a vertically sheared environment. Preprints, *25th Conf. on Severe Local Storms*, Denver, CO, Amer. Meteor. Soc., 15.1. [Available online at http://ams.confex.com/ams/25SLS/techprogram/paper_176112.htm.]
- , —, —, J. Marquis, and J. Wurman, 2011: Characteristics of the wind field in three nontornadic low-level mesocyclones observed by the Doppler on Wheels radars. *Electron. J. Severe Storms Meteor.*, **6** (3).
- , and Coauthors, 2012: The pretornadic phase of the Goshen County, Wyoming, supercell of 5 June 2009 intercepted by VORTEX2. Part II: Intensification of low-level rotation. *Mon. Wea. Rev.*, **140**, 2916–2938.
- Marquis, J., Y. Richardson, J. Wurman, P. Markowski, and D. Dowell, 2008: Mobile radar observations of tornadic supercells with multiple rear-flank gust fronts. Preprints, *24th Conf. on Severe Local Storms*, Savannah, GA, Amer. Meteor. Soc., 19.3. [Available online at http://ams.confex.com/ams/24SLS/techprogram/paper_142112.htm.]
- , —, P. Markowski, D. Dowell, and J. Wurman, 2012: Tornado maintenance investigated with high-resolution dual-Doppler and EnKF analysis. *Mon. Wea. Rev.*, **140**, 3–27.
- Okubo, A., 1970: Horizontal dispersion of floatable particles in the vicinity of velocity singularities such as convergences. *Deep-Sea Res.*, **17**, 445–454.
- Pauley, P. M., and X. Wu, 1990: The theoretical, discrete, and actual response of the Barnes objective analysis scheme for one- and two-dimensional fields. *Mon. Wea. Rev.*, **118**, 1145–1163.

- Rasmussen, E. N., J. M. Straka, M. S. Gilmore, and R. Davies-Jones, 2006: A preliminary survey of rear-flank descending reflectivity cores in supercell storms. *Wea. Forecasting*, **21**, 923–938.
- Ray, P. S., C. L. Ziegler, W. Bumgarner, and R. J. Serafin, 1980: Single- and multiple-Doppler radar observations of tornadic storms. *Mon. Wea. Rev.*, **108**, 1607–1625.
- Shabbott, C. J., and P. M. Markowski, 2006: Surface in situ observations within the outflow of forward-flank downdrafts of supercell thunderstorms. *Mon. Wea. Rev.*, **134**, 1422–1441.
- Straka, J. M., E. N. Rasmussen, and S. E. Fredrickson, 1996: A mobile mesonet for fine-scale meteorological observations. *J. Atmos. Oceanic Technol.*, **13**, 921–936.
- , —, R. P. Davies-Jones, and P. M. Markowski, 2007: An observational and idealized numerical examination of low-level counter-rotating vortices toward the rear flank of supercells. *Electron. J. Severe Storms Meteor.*, **2** (8).
- Trapp, R. J., and C. A. Doswell, 2000: Radar data objective analysis. *J. Atmos. Oceanic Technol.*, **17**, 105–120.
- Wakimoto, R. M., N. T. Atkins, and J. Wurman, 2011: The LaGrange tornado during VORTEX2. Part I: Photogrammetric analysis of the tornado combined with single-Doppler radar data. *Mon. Wea. Rev.*, **139**, 2233–2258.
- Wagh, S., and S. E. Fredrickson, 2010: An improved aspirated temperature system for mobile meteorological observations, especially in severe weather. Preprints, *25th Conf. on Severe Local Storms*, Denver, CO, Amer. Meteor. Soc., P5.2. [Available online at http://ams.confex.com/ams/25SLS/techprogram/paper_176205.htm.]
- Weiss, C. C., and J. L. Schroeder, 2008: StickNet—A new portable, rapidly deployable, surface observing system. Preprints, *24th Conf. on Interactive Information and Processing Systems*, New Orleans, LA, Amer. Meteor. Soc., 4A.1. [Available online at http://ams.confex.com/ams/88Annual/techprogram/paper_134047.htm.]
- Weiss, J., 1991: The dynamics of enstrophy transfer in two-dimensional hydrodynamics. *Physica D*, **48**, 273–294.
- Wurman, J., J. Straka, E. Rasmussen, M. Randall, and A. Zahrai, 1997: Design and deployment of a portable, pencil-beam, pulsed, 3-cm Doppler radar. *J. Atmos. Oceanic Technol.*, **14**, 1502–1512.
- , Y. Richardson, C. Alexander, S. Weygandt, and P. F. Zhang, 2007: Dual-Doppler and single-Doppler analysis of a tornadic storm undergoing mergers and repeated tornadogenesis. *Mon. Wea. Rev.*, **135**, 736–758.
- , K. Kosiba, P. Markowski, Y. Richardson, and D. Dowell, 2010: Finescale single- and dual-Doppler analysis of tornado intensification, maintenance, and dissipation in the Orleans, Nebraska, tornadic supercell. *Mon. Wea. Rev.*, **138**, 4439–4455.
- , D. Dowell, Y. Richardson, P. Markowski, E. Rasmussen, D. Burgess, L. Wicker, and H. Bluestein, 2012: The Second Verification of the Origins of Rotation in Tornadoes Experiment: VORTEX2. *Bull. Amer. Meteor. Soc.*, **93**, 1147–1170.